Chinese Journal of Aeronautics, (2014),27(2): 299–312

Chinese Society of Aeronautics and Astronautics
& Beihang University

Chinese Journal of Aeronautics

cja@buaa.edu.cn
www.sciencedirect.com

Deploying process modeling and attitude control of a satellite with a large deployable antenna

Zhigang Xing, Gangtie Zheng *

School of Aerospace, Tsinghua University, Beijing 100084, China

Received 26 April 2013; revised 26 June 2013; accepted 15 July 2013
Available online 25 February 2014

KEYWORDS

Attitude control;
Communication satellite;
Deploying process modeling;
Disturbance rejection;
Large deployable antenna

Abstract Modeling and attitude control methods for a satellite with a large deployable antenna are studied in the present paper. Firstly, for reducing the model dimension, three dynamic models for the deploying process are developed, which are built with the methods of multi-rigid-body dynamics, hybrid coordinate and substructure. Then an attitude control method suitable for the deploying process is proposed, which can keep stability under any dynamical parameter variation. Subsequently, this attitude control is optimized to minimize attitude disturbance during the deploying process. The simulation results show that this attitude control method can keep stability and maintain proper attitude variation during the deploying process, which indicates that this attitude control method is suitable for practical applications.

1. Introduction

Over the past two decades, great strides have been made in the area of large space structures such as communication antennae,[1–4] solar sails,[5–7] space-based radars,[8] telescope reflectors,[9] etc. The sizes of these deployable structures could be larger than one hundred meters in the near future with extreme lightweight and flexibility. Therefore, a deployable design is always necessary for folding a structure to fit the space of fairing during the launch stage and deploying it to a designed configuration in orbit. Apparently, the deploying process is the key phase of such a mission with large deployable structures. In this phase, the inertia tensor, the structural frequency, and the coupling coefficients change widely under the influences of some uncertain factors, such as manufacture errors of deployment mechanism, impact torque, and space environment torque.[10] During this phase, the attitude of the satellite is critical to the mission. If an active attitude control is not performed during this phase, the attitude benchmark of the satellite may be lost, even the spacecraft would roll out of control, resulting in severe mission risks.

An effective approach toward solving this problem is to control the satellite attitude during the deploying process to restrict the attitude variation in a certain range. As a foundation of attitude control, a proper dynamic model should be established first, which is often considered as a space structure modeling problem. For the modeling problem, the hybrid coordinate modeling method[11] proposed by Likins is widely used, which utilizes the rigid-body coordinate and the modal coordinate to describe the rigid-body attitude motion and the flexible vibration, respectively. This method has been successfully applied in modeling many satellites.[7,12–16] However, a

* Corresponding author. Tel.: +86 10 62783235.
E-mail addresses: roosevelt980343@gmail.com (Z. Xing), gtzheng@mail.tsinghua.edu.cn (G. Zheng).

Peer review under responsibility of Editorial Committee of CJA.

Production and hosting by Elsevier

1000-9361 © 2014 Production and hosting by Elsevier Ltd. on behalf of CSAA & BUAA. Open access under CC BY-NC-ND license.
http://dx.doi.org/10.1016/j.cja.2014.02.004

satellite's configuration changes continually during the deploying process of a space structure, so directly applying the hybrid coordinate modeling method will generate a huge amount of computation cost as the finite element model has to be built for each possible configuration with subsequent modal analyses for each model. Therefore, some alternative methods have been proposed. Taking into account an important fact that the only change to a single component during the deploying process is its relative location to other components instead of itself, the component modal synthesis method[17] finds its application value here. At present, this synthesis method has been applied to the modeling of large spacecraft with complex configurations,[18,19] especially for the International Space Station.[20,21] However, no reports have been found for its application in modeling the space structure deploying process.

The attitude control problem for the space structure deploying process can be classified as the space flexible structure attitude control problem. There are many researches in this area. In 1990s, NASA proposed the Controls-Structures Interaction (CSI) research project, resulting in some new design theories for flexible structure attitude control,[22] which included the state space based modern design and the frequency domain based classical design. Due to its good adaptability to uncertain parameters, the H_∞ design method has been addressed by many researchers.[15,23–25] With the consideration of maturity and reliability, the frequency domain based classical approaches are still widely used in the attitude control of flexible spacecraft,[13,16,26,27] while the robust attitude control design (H_∞ approach) has been validated by in-orbit experiments[12,14] and applied in the SB4000 platform.[28] Currently, there are 15 SB4000-based satellites in the orbit. However, the attitude control for the space structure deploying process, which is a critical phase of a mission, has not been studied so extensively.

In this paper, the deploying process dynamic modeling and attitude control of a large deployable antenna are discussed. For the deploying process modeling problem, to obtain a proper and practically applicable dynamic model, a multi-model strategy is developed. With these models, the attitude control method for the deploying process is investigated in detail. Finally, the numerical simulation results of the deploying process attitude control are presented.

2. Deploying process modeling

2.1. Deploying process description

The deploying process of a large deployable antenna is somewhat complicated, which includes five steps: big arm deploying

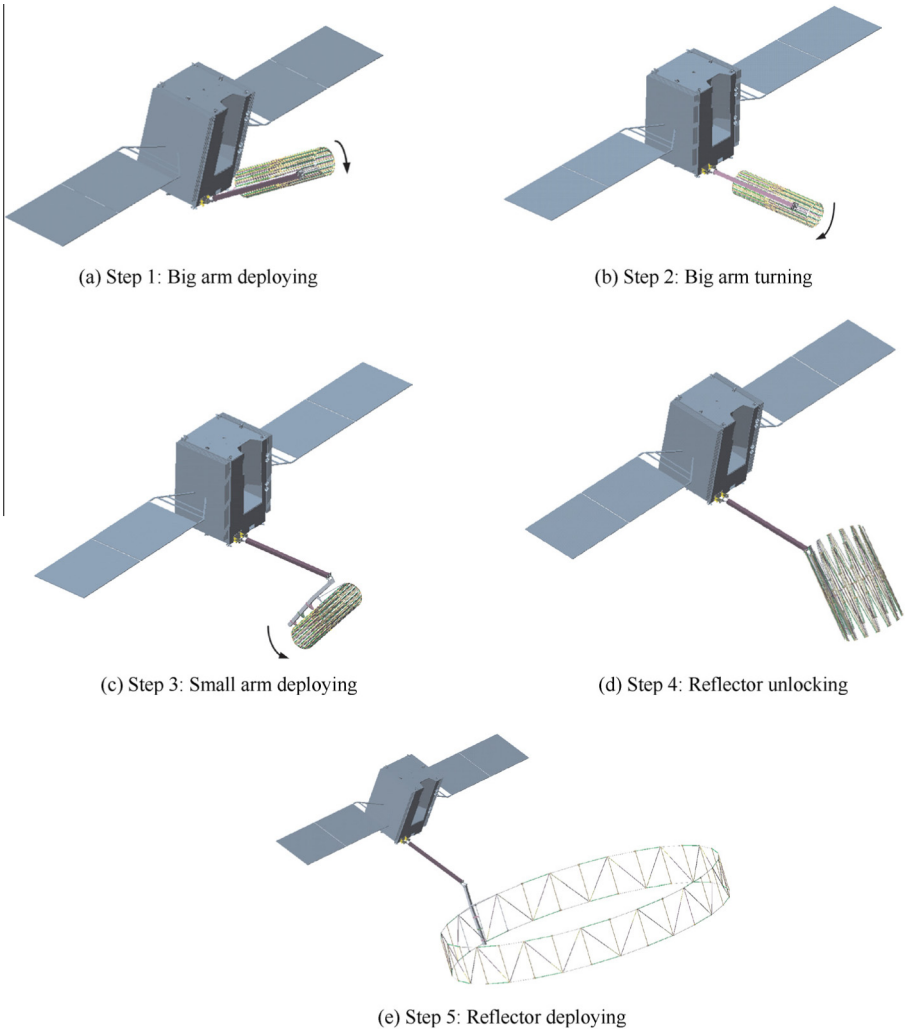

Fig. 1 Deploying process of a large deployable antenna.

(Fig. 1(a)), big arm turning (Fig. 1(b)), small arm deploying (Fig. 1(c)), reflector unlocking (Fig. 1(d)), and reflector deploying (Fig. 1(e)). Divided between the third step (small arm deploying) and the fourth step (reflector unlocking), the whole deploying process can be considered as two phases, i.e., the arm deploying phase and the reflector deploying phase. In order to perform the control design and the computer simulation of the deploying process, it is necessary to build its dynamic model. For the computer simulation, the model should be capable of describing the process, which is basically a dynamic process, as accurate as possible. On the other hand, the model should be practically applicable to the control design and hence has a low order. However, due to the complexity of this procedure, it is difficult to build a model to simultaneously satisfy these two different requirements. For coping with this problem, a proper modeling strategy is necessary.

According to the primary features of the deploying process (wide range variations of the inertia tensor, the structural frequencies, and the rotational coupling coefficients), a three-aspect modeling strategy of this deploying process is suggested as follows. Firstly, to characterize the wide variation of the inertia tensor, a multi-rigid-body dynamic model including both the arm deploying phase and the reflector deploying phase is established with the assistance of commercially available multi-body dynamics software. With this software, which is used for simulating the inertia tensor's wide variation, and the control design/simulation software, we take the approach of multi-body dynamics and attitude control interactive simulation to validate the control design in the whole deploying process. Secondly, to characterize the wide variations of the structural frequencies and the rotational coupling coefficients during the arm deploying phase, a composite flexible dynamic model is established using the substructure method and the hybrid coordinates. This model can describe the arm deploying phase analytically. The third aspect is to select several typical working points in the reflector deploying phase to characterize the deploying phase and set up several flexible dynamic models corresponding to some typical deploying steps in the reflector deploying phase, which can approximately describe the wide range parameter variations.

2.2. Multi-rigid-body dynamic modeling

With the commercially available multi-body dynamics software and its interface to the computer aided design (CAD) software, all the moving elements in the deploying process can be modeled. Then, according to the motion properties of the deploying process, 278 constraints are added to the model, including hinge, translation, fix, etc. Next, the forces and torques during the deploying process are defined (except for the driving cable force), including torsion spring force, bushing force, contact friction force, etc. There are totally 375 forces and torques added in all. In this way, a basic multi-rigid-body dynamic model is established. In the steps of reflector unlocking and reflector deploying, the unlocking and locking procedures in the dynamic model are considered as changes of the constraints. Thus, the complicated whole deploying process (including Steps 1-5) can be modeled with the established model of multi-rigid-body dynamics.

In the step of reflector deploying, the antenna truss deploys under the traction of the driving cable as shown in Fig. 2. As an indispensable part, it is necessary to establish a dynamic model for this driving cable. Undoubtedly, during the in-orbit reflector deploying process, the tension force is the main force applied to the driving cable. Therefore, the driving cable is in a tensioned state. As the force in the driving cable should approximately satisfy the Hooke theorem, for a deployable unit of the antenna truss, the driving cable and the deploying mechanism can be simplified as shown in Fig. 3(a). During the reflector deploying, the chain wheel rotates and the cable's friction and pressure force drive the reflector truss to deploy as illustrated in Fig. 3(b).

According to classical Palmgrem empirical formulae, the friction torque M on the chain wheel bearing can be expressed as

$$M = f_1 F_\beta d_\mathrm{m} \tag{1}$$

where f_1 is a coefficient, F_β is the composite torque load, which approximately equals the radial force F_γ of the ball bearing, and d_m is the bearing diameter. Let $f = f_1 d_\mathrm{m}$, Eq. (1) can be rewritten as

$$M = f F_\gamma \tag{2}$$

The dynamic equations of the chain wheel could be written as

$$\boldsymbol{T}_n + \boldsymbol{T}_{n+1} + \boldsymbol{F}_\gamma - m\boldsymbol{a}_\mathrm{c} = \boldsymbol{0} \tag{3}$$

$$\boldsymbol{R}_n \times \boldsymbol{T}_n + \boldsymbol{R}_{n+1} \times \boldsymbol{T}_{n+1} + \boldsymbol{M} - \frac{1}{2} m \mid \boldsymbol{R}_i \mid^2 \frac{\mathrm{d}\boldsymbol{\omega}}{\mathrm{d}t} = \boldsymbol{0} \tag{4}$$

where m, $\boldsymbol{a}_\mathrm{c}$, and $\boldsymbol{\omega}$ represent the mass of the chain wheel, the acceleration of the chain wheel's mass center, and the angular velocity of the chain wheel, respectively. Here $\boldsymbol{R}_n$ is the vector from the chain wheel center to the action point of the tension

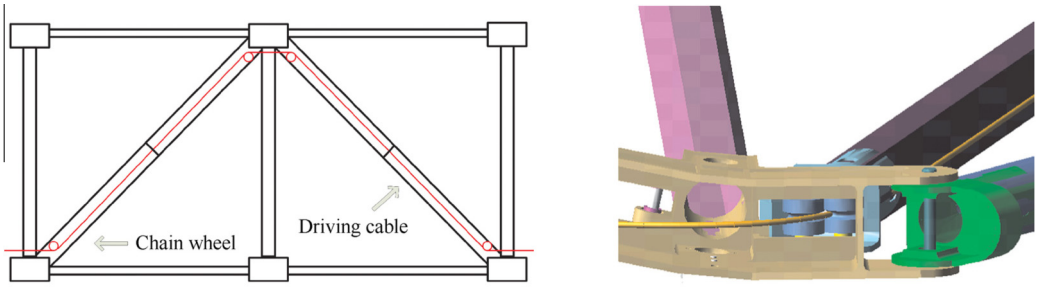

(a) Diagrammatic sketch (b) Engineering drawing

Fig. 2 Reflector deploying driving cable.

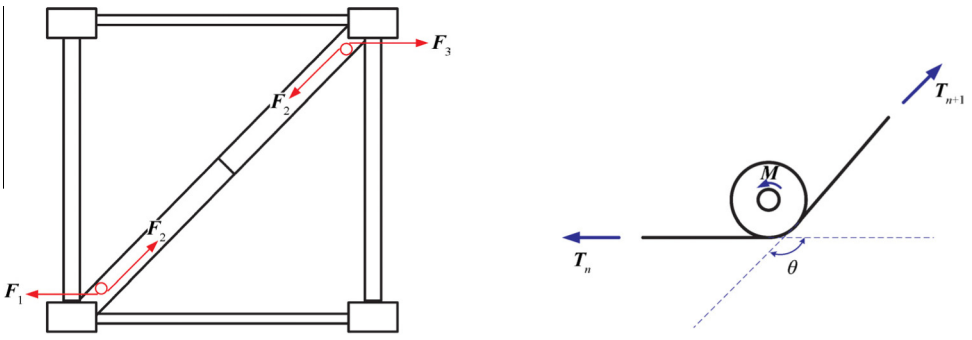

(a) Overall drawing (b) Part drawing

Fig. 3 A simplified model of the driving cable.

force $\boldsymbol{T}_n$, and M corresponds to the magnitude of the vector $\boldsymbol{M}$, so as the other vectors. For a specific antenna, m and $|\boldsymbol{R}_i|$ are 4.43×10^{-3} kg and 13.7×10^{-3} m, respectively.

Considering the fact that a typical tension force is 10^3 N and $\boldsymbol{a}_c$ is relatively small in a practical deploying process, Eq. (3) could be approximately simplified as

$$\boldsymbol{T}_n + \boldsymbol{T}_{n+1} + \boldsymbol{F}_\gamma = \boldsymbol{0} \tag{5}$$

Similarly, because $|\boldsymbol{R}_i|$ and $\dot{\boldsymbol{\omega}}$ are also relatively small, Eq. (4) could also be simplified as

$$\boldsymbol{R}_n \times \boldsymbol{T}_n + \boldsymbol{R}_{n+1} \times \boldsymbol{T}_{n+1} + \boldsymbol{M} = \boldsymbol{0} \tag{6}$$

The essence of this simplification is to neglect the inertia of the chain wheel. In a large deployable antenna, the chain wheel is so small and light that the simplification is proper and acceptable.

According to Eq. (5), there is

$$F_\gamma^2 = T_n^2 + T_{n+1}^2 + 2T_nT_{n+1}\cos\theta \tag{7}$$

and from Eq. (6), another relation is derived as

$$(T_n - T_{n+1})R - fF_\gamma = 0 \tag{8}$$

where R represents the magnitude of $\boldsymbol{R}_i$. From Eqs. (7) and (8), one can have

$$(T_n - T_{n+1})R - f\sqrt{T_n^2 + T_{n+1}^2 + 2T_nT_{n+1}\cos\theta} = 0 \tag{9}$$

which is the dynamic model of the driving cable.

In Eq. (9), for a given T_n, the subsequent cable force T_{n+1} can be calculated. Thus, if the initial force T_1 is given (by the electric motor), all the cable forces in the reflector can be calculated during the reflector deploying process. However, each calculation with Eq. (9) needs to solve a quadratic equation, which complicates the calculation and decreases the calculation accuracy and efficiency. Therefore, a further simplification is required. For one ball bearing, the cable force on each side is nearly the same, i.e., T_n and T_{n+1} are almost the same. From Eq. (9) and the trigonometric function formula, a further simplified cable dynamic model can be obtained, which is

$$T_{n+1} = \frac{R - f\cos\frac{\theta}{2}}{R + f\cos\frac{\theta}{2}}T_n \tag{10}$$

The simplified cable dynamic model of Eq. (10) can be validated by comparing the results calculated using Eq. (9) and Eq. (10) with the typical values of parameters and forces, where R is 0.0137 m, f is 6×10^{-4} m, θ is 120°, and T_n is 1000 N. With Eq. (9), the cable tension force T_{n+1} is 957.1127 N, whereas T_{n+1} is 957.1428 N by Eq. (10). Therefore, this simplified cable dynamic model is usable.

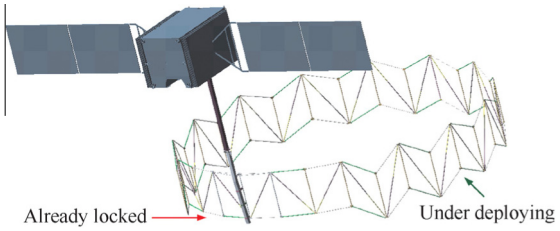

Fig. 4 Unsynchronized phenomenon in the reflector deploying phase.

In the subsequent simulation, the unsynchronized phenomenon in the practical ground deploying test can be generated with the dynamic model and thus built as shown in Fig. 4, which also validates the model's reliability and accuracy.

2.3. Composite flexible dynamic modeling for the arm deploying phase

Except for the inertia tensor, the structural frequencies and the rotational coupling coefficients also change widely in the arm deploying phase, which cannot be characterized by the multi-rigid-body model established above. Therefore, for this phase, a composite flexible dynamic model is developed with the substructure method and the hybrid coordinates. The related coordinate frames and vectors are defined as shown in Fig. 5 and listed in Table 1.

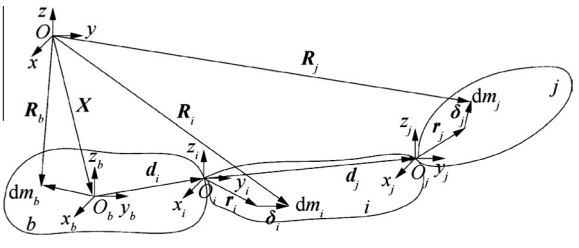

Fig. 5 Sketch map of the deployable arm deploying phase.

Table 1 Coordinate frame description.

Coordinate	Description
$Oxyz$	The inertial coordinate frame, simplified as o frame
$O_bx_by_bz_b$	The satellite bus frame with the origin located at the satellite mass center, simplified as b frame
$O_ix_iy_iz_i$	The first-stage flexible appendage i (big arm) frame, simplified as i frame
$O_jx_jy_jz_j$	The second-stage flexible appendage j (small arm and reflector) frame, simplified as j frame

For a point on the satellite bus b, its location in the inertial space is

$$\boldsymbol{R}_b = \boldsymbol{X} + \boldsymbol{r}_b \tag{11}$$

in which $\boldsymbol{X}$ is the displacement of the satellite bus mass center and $\boldsymbol{r}_b$ is the vector from O_b to this point. Thus, the velocity of this point can be expressed as

$$\dot{\boldsymbol{R}}_b = \boldsymbol{C}_o^b \dot{\boldsymbol{X}} + \tilde{\boldsymbol{r}}_b^{\mathrm{T}} \boldsymbol{\omega}_{\mathrm{s}} \tag{12}$$

where $\boldsymbol{C}_o^b$ is the transformation matrix from o frame to b frame, $\tilde{\boldsymbol{r}}_b$ the external product matrix of the vector $\boldsymbol{r}_b$ with " $\sim$ " being the external product sign, and $\boldsymbol{\omega}_{\mathrm{s}}$ the angular velocity vector of the satellite bus. Then the kinetic energy of the satellite bus b can be written as

$$\begin{aligned} T_b &= \frac{1}{2}\int_b \dot{\boldsymbol{R}}_b^{\mathrm{T}} \dot{\boldsymbol{R}}_b \mathrm{d}m \\ &= \frac{1}{2} M_b \dot{\boldsymbol{X}}^{\mathrm{T}} \dot{\boldsymbol{X}} + \dot{\boldsymbol{X}}^{\mathrm{T}} \left(\sum_b m_b \boldsymbol{C}_o^{b\mathrm{T}} \tilde{\boldsymbol{r}}_b^{\mathrm{T}} \right) \boldsymbol{\omega}_{\mathrm{s}} + \frac{1}{2} \boldsymbol{\omega}_{\mathrm{s}}^{\mathrm{T}} \left(\sum_b m_b \tilde{\boldsymbol{r}}_b \tilde{\boldsymbol{r}}_b^{\mathrm{T}} \right) \boldsymbol{\omega}_{\mathrm{s}} \end{aligned} \tag{13}$$

where M_b is the mass of the satellite bus and m_b the mass of the point. There is no elastic potential energy in the satellite bus (rigid-body).

For a point on the first-stage flexible appendage i, its location in the inertial space is defined as

$$\boldsymbol{R}_i = \boldsymbol{X} + \boldsymbol{d}_i + \boldsymbol{r}_i + \boldsymbol{\delta}_i \tag{14}$$

where $\boldsymbol{d}_i$ is the vector from O_b to O_i, $\boldsymbol{r}_i$ is the vector from O_i to $\mathrm{d}m_i$ shown in Fig. 5, and $\boldsymbol{\delta}_i$ is the deformation displacement of $\mathrm{d}m_i$. In the modal space, $\boldsymbol{\delta}_i$ can be expressed as

$$\boldsymbol{\delta}_i = \{\boldsymbol{i}\}^{\mathrm{T}} \boldsymbol{\Phi}_{i\mathrm{t}} \boldsymbol{\eta}_i \tag{15}$$

where $\{\boldsymbol{i}\}$ is the basic vector of the i frame, $\boldsymbol{\Phi}_{i\mathrm{t}}$ is the normal modes matrix of the first-stage flexible appendage i, which only includes the translational modes, and $\boldsymbol{\eta}_i$ is the corresponding modal coordinate.

Let

$$\boldsymbol{A}_i = \boldsymbol{C}_b^i \boldsymbol{C}_o^b \tag{16}$$

$$\boldsymbol{B}_i = \boldsymbol{C}_b^i \tilde{\boldsymbol{d}}_i^{\mathrm{T}} + \tilde{\boldsymbol{r}}_i^{\mathrm{T}} \boldsymbol{C}_b^i \tag{17}$$

The velocity of this point is

$$\dot{\boldsymbol{R}}_i = \boldsymbol{C}_b^i \boldsymbol{C}_o^b \dot{\boldsymbol{X}} + \boldsymbol{B}_i \boldsymbol{\omega}_{\mathrm{s}} + \tilde{\boldsymbol{r}}_i^{\mathrm{T}} \boldsymbol{\omega}_i + \dot{\boldsymbol{\delta}}_i \tag{18}$$

where $\boldsymbol{C}_b^i$ is the transformation matrix from the b frame to the i frame, $\tilde{\boldsymbol{d}}_i$ is the external product matrix of the vector $\boldsymbol{d}_i$, and $\boldsymbol{\omega}_i$ is the angular velocity vector of the first-stage flexible appendage i. Thus the kinetic energy of the first-stage flexible appendage i can be expressed as

$$\begin{aligned} T_i &= \frac{1}{2}\int_i \dot{\boldsymbol{R}}_i^{\mathrm{T}} \dot{\boldsymbol{R}}_i \mathrm{d}m \\ &= \frac{1}{2} M_i \dot{\boldsymbol{X}}^{\mathrm{T}} \dot{\boldsymbol{X}} + \dot{\boldsymbol{X}}^{\mathrm{T}} \left(\sum_i m_i \boldsymbol{A}_i^{\mathrm{T}} \boldsymbol{B}_i \right) \boldsymbol{\omega}_{\mathrm{s}} + \dot{\boldsymbol{X}}^{\mathrm{T}} \left(\sum_i m_i \boldsymbol{A}_i^{\mathrm{T}} \tilde{\boldsymbol{r}}_i^{\mathrm{T}} \right) \boldsymbol{\omega}_i \\ &\quad + \dot{\boldsymbol{X}}^{\mathrm{T}} \left(\sum_i m_i \boldsymbol{A}_i^{\mathrm{T}} \boldsymbol{\Phi}_{i\mathrm{t}} \dot{\boldsymbol{\eta}}_i \right) \\ &\quad + \frac{1}{2} \boldsymbol{\omega}_{\mathrm{s}}^{\mathrm{T}} \left(\sum_i m_i \boldsymbol{B}_i^{\mathrm{T}} \boldsymbol{B}_i \right) \boldsymbol{\omega}_{\mathrm{s}} + \boldsymbol{\omega}_{\mathrm{s}}^{\mathrm{T}} \left(\sum_i m_i \boldsymbol{B}_i^{\mathrm{T}} \tilde{\boldsymbol{r}}_i^{\mathrm{T}} \right) \boldsymbol{\omega}_i \\ &\quad + \boldsymbol{\omega}_{\mathrm{s}}^{\mathrm{T}} \left(\sum_i m_i \boldsymbol{B}_i^{\mathrm{T}} \boldsymbol{\Phi}_{i\mathrm{t}} \dot{\boldsymbol{\eta}}_i \right) \\ &\quad + \frac{1}{2} \boldsymbol{\omega}_i^{\mathrm{T}} \left(\sum_i m_i \tilde{\boldsymbol{r}}_i \tilde{\boldsymbol{r}}_i^{\mathrm{T}} \right) \boldsymbol{\omega}_i + \boldsymbol{\omega}_i^{\mathrm{T}} \left(\sum_i m_i \tilde{\boldsymbol{r}}_i \boldsymbol{\Phi}_{i\mathrm{t}} \dot{\boldsymbol{\eta}}_i \right) \\ &\quad + \frac{1}{2} \sum_i m_i \dot{\boldsymbol{\eta}}_i^{\mathrm{T}} \boldsymbol{\Phi}_{i\mathrm{t}}^{\mathrm{T}} \boldsymbol{\Phi}_{i\mathrm{t}} \dot{\boldsymbol{\eta}}_i \end{aligned} \tag{19}$$

where M_i is the mass of the first-stage flexible appendage i and m_i the mass of the point. Different from the satellite bus, the first-stage flexible appendage i has its elastic potential energy, which is

$$V_i = \frac{1}{2} \boldsymbol{\eta}_i^{\mathrm{T}} \boldsymbol{\Phi}_i^{\mathrm{T}} \boldsymbol{K}_{\mathrm{nn}}^i \boldsymbol{\Phi}_i \boldsymbol{\eta}_i = \frac{1}{2} \boldsymbol{\eta}_i^{\mathrm{T}} \boldsymbol{\Lambda}_i \boldsymbol{\eta}_i \tag{20}$$

where $\boldsymbol{K}_{\mathrm{nn}}^i$ is the stiffness matrix of the first-stage flexible appendage i, $\boldsymbol{\Phi}_i$ is the normal modes matrix under the constrained boundary condition, and $\boldsymbol{\Lambda}_i$ is the eigenvalue matrix under the constrained boundary condition.

For a point on the second-stage flexible appendage j, its location in the inertial space can be expressed as

$$\boldsymbol{R}_j = \boldsymbol{X} + \boldsymbol{d}_i + \boldsymbol{d}_j + \boldsymbol{r}_j + \boldsymbol{\delta}_j \tag{21}$$

where $\boldsymbol{d}_j$ is the vector from O_i to O_j, $\boldsymbol{r}_j$ is the vector from O_j to $\mathrm{d}m_j$, and $\boldsymbol{\delta}_j$ is the deformation displacement of $\mathrm{d}m_j$, which is caused by two factors which are the deformation of the first-stage flexible appendage i (boundary displacement) and the deformation of the second-stage flexible appendage j itself. In the modal space, $\boldsymbol{\delta}_j$ can have the form as

$$\boldsymbol{\delta}_j = \{\boldsymbol{j}\}^{\mathrm{T}} \boldsymbol{\Phi}_{j\mathrm{t}} \boldsymbol{\eta}_j + \{\boldsymbol{j}\}^{\mathrm{T}} \boldsymbol{\Psi}_{j\mathrm{t}} \boldsymbol{\varepsilon}_j \tag{22}$$

where $\{\boldsymbol{j}\}$ is the basic vector of the j frame, $\boldsymbol{\Phi}_{j\mathrm{t}}$ is the normal modes matrix of the second-stage flexible appendage j which only includes the translational modes, $\boldsymbol{\eta}_j$ is the corresponding modal coordinate, $\boldsymbol{\Psi}_{j\mathrm{t}}$ is the constraint mode matrix, and $\boldsymbol{\varepsilon}_j$ is the boundary DOF corresponding to $\boldsymbol{\Psi}_{j\mathrm{t}}$.

In order to obtain $\boldsymbol{\Psi}_{j\mathrm{t}}$, one should find the internal displacement $\boldsymbol{r}_{ji}$ of the appendage j caused by the boundary DOF's unit rotation in the O_jx_j direction

$$\boldsymbol{r}_{ji} = \frac{\boldsymbol{x}_j}{|\boldsymbol{x}_j|} \times \boldsymbol{r}_j \tag{23}$$

which can also have the form of

$$\{\boldsymbol{j}\}^{\mathrm{T}} \boldsymbol{r}_{ji} = \{\boldsymbol{j}\}^{\mathrm{T}} \frac{\boldsymbol{x}_j}{|\boldsymbol{x}_j|} \times \boldsymbol{r}_j \tag{24}$$

where

$$\boldsymbol{r}_{ji} = \begin{bmatrix} r_{jix} \\ r_{jiy} \\ r_{jiz} \end{bmatrix} = \frac{\boldsymbol{x}_j}{|\boldsymbol{x}_j|} \times \boldsymbol{r}_j \tag{25}$$

In fact, because $\frac{\boldsymbol{x}_j}{|\boldsymbol{x}_j|}$ is a unit vector, there is

$$\frac{\boldsymbol{x}_j}{|\boldsymbol{x}_j|} = \begin{bmatrix} 1 \\ 0 \\ 0 \end{bmatrix} \tag{26}$$

With Eqs. (25) and (26), the internal displacement $\boldsymbol{r}_{ji}$ can be obtained.

With the same approach, the internal displacement $\boldsymbol{r}_{jj}$ of the appendage j caused by the boundary DOF's unit rotation along the O_jy_j direction can be expressed as

$$\boldsymbol{r}_{jj} = \begin{bmatrix} r_{jjx} \\ r_{jjy} \\ r_{jjz} \end{bmatrix} = \frac{\boldsymbol{y}_j}{|\boldsymbol{y}_j|} \times \boldsymbol{r}_j \tag{27}$$

Since $\frac{\boldsymbol{y}_j}{|\boldsymbol{y}_j|}$ is also a unit vector, there is

$$\frac{\boldsymbol{y}_j}{|\boldsymbol{y}_j|} = \begin{bmatrix} 0 \\ 1 \\ 0 \end{bmatrix} \tag{28}$$

and thus the internal displacement $\boldsymbol{r}_{jj}$ can be obtained from Eqs. (27) and (28).

Similarly, the internal displacement $\boldsymbol{r}_{jk}$ of the appendage j caused by the boundary DOF's unit rotation along the O_jz_j direction can be expressed as

$$\boldsymbol{r}_{jk} = \begin{bmatrix} r_{jkx} \\ r_{jky} \\ r_{jkz} \end{bmatrix} = \frac{\boldsymbol{z}_j}{|\boldsymbol{z}_j|} \times \boldsymbol{r}_j \tag{29}$$

Because $\frac{\boldsymbol{z}_j}{|\boldsymbol{z}_j|}$ is a unit vector, there is

$$\frac{\boldsymbol{z}_j}{|\boldsymbol{z}_j|} = \begin{bmatrix} 0 \\ 0 \\ 1 \end{bmatrix} \tag{30}$$

According to Eqs. (29) and (30), the internal displacement $\boldsymbol{r}_{jk}$ can be obtained.

With Eqs. (25)–(30), the constraint mode matrix $\boldsymbol{\Psi}_{j\mathrm{t}}$ can be given by

$$\boldsymbol{\Psi}_{j\mathrm{t}} = \begin{bmatrix} 1 & 0 & 0 & r_{jix} & r_{jjx} & r_{jkx} \\ 0 & 1 & 0 & r_{jiy} & r_{jjy} & r_{jky} \\ 0 & 0 & 1 & r_{jiz} & r_{jjz} & r_{jkz} \end{bmatrix} \tag{31}$$

The joint point O_j, which connects the first-stage flexible appendage i and the second-stage flexible appendage j, can be considered as a point of the flexible appendage i, and thus

$$\{\boldsymbol{j}\}^{\mathrm{T}}\boldsymbol{\varepsilon}_j = \{\boldsymbol{i}\}^{\mathrm{T}}\boldsymbol{\delta}_{i^*} = \{\boldsymbol{j}\}^{\mathrm{T}}\boldsymbol{Q}_i^j\boldsymbol{\delta}_{i^*} = \{\boldsymbol{j}\}^{\mathrm{T}}\boldsymbol{Q}_i^j\boldsymbol{\Phi}_{i^*}\boldsymbol{\eta}_i \tag{32}$$

where $\boldsymbol{\delta}_{i^*}$ is the O_j's deformation presenting in the flexible appendage i, $\boldsymbol{\Phi}_{i^*}$ is the O_j's normal modes matrix under the fixed boundary condition, and

$$\boldsymbol{Q}_i^j = \mathrm{diag}(\boldsymbol{C}_i^j, \boldsymbol{C}_i^j) \tag{33}$$

where $\boldsymbol{C}_i^j$ is the transformation matrix from the i frame to the j frame.

According to Eqs. (22), (31), and (32), $\boldsymbol{\delta}_j$ can be expressed as

$$\boldsymbol{\delta}_j = \{\boldsymbol{j}\}^{\mathrm{T}}\boldsymbol{\Phi}_{j\mathrm{t}}\boldsymbol{\eta}_j + \{\boldsymbol{j}\}^{\mathrm{T}}\boldsymbol{\Psi}_{j\mathrm{t}}\boldsymbol{Q}_i^j\boldsymbol{\Phi}_{i^*}\boldsymbol{\eta}_i \tag{34}$$

Let

$$\boldsymbol{B}_j = \boldsymbol{C}_i^j\boldsymbol{C}_b^i\tilde{\boldsymbol{d}}_i^{\mathrm{T}} + \boldsymbol{C}_i^j\tilde{\boldsymbol{d}}_j^{\mathrm{T}}\boldsymbol{C}_b^i + \tilde{\boldsymbol{r}}_j^{\mathrm{T}}\boldsymbol{C}_i^j\boldsymbol{C}_b^i \tag{35}$$

$$\boldsymbol{D}_j = \boldsymbol{C}_i^j\tilde{\boldsymbol{d}}_j^{\mathrm{T}} + \tilde{\boldsymbol{r}}_j^{\mathrm{T}}\boldsymbol{C}_i^j \tag{36}$$

The velocity of a point on the appendage j can be expressed as

$$\dot{\boldsymbol{R}}_j = \boldsymbol{C}_i^j\boldsymbol{C}_b^i\boldsymbol{C}_o^b\dot{\boldsymbol{X}} + \boldsymbol{B}_j\boldsymbol{\omega}_{\mathrm{s}} + \boldsymbol{D}_j\boldsymbol{\omega}_i + \tilde{\boldsymbol{r}}_j^{\mathrm{T}}\boldsymbol{\omega}_j + \boldsymbol{\Phi}_{j\mathrm{t}}\dot{\boldsymbol{\eta}}_j + \boldsymbol{\Psi}_{j\mathrm{t}}\boldsymbol{Q}_i^j\boldsymbol{\Phi}_{i^*}\dot{\boldsymbol{\eta}}_i \tag{37}$$

where $\tilde{\boldsymbol{d}}_j$ is the external product matrix of the vector $\boldsymbol{d}_j$, $\tilde{\boldsymbol{r}}_j$ the external product matrix of the vector $\boldsymbol{r}_j$, and $\boldsymbol{\omega}_j$ the angular velocity vector of the second-stage flexible appendage j relative to the first-stage flexible appendage i. Thus, one can have the kinetic energy of the second-stage flexible appendage j:

$$\begin{aligned}
T_j &= \frac{1}{2}\int_j \dot{\boldsymbol{R}}_j^{\mathrm{T}}\boldsymbol{R}_j\mathrm{d}m \\
&= \frac{1}{2}M_j\dot{\boldsymbol{X}}^{\mathrm{T}}\dot{\boldsymbol{X}} + \dot{\boldsymbol{X}}^{\mathrm{T}}\left(\sum_j m_j\boldsymbol{A}_j^{\mathrm{T}}\boldsymbol{B}_j\right)\boldsymbol{\omega}_{\mathrm{s}} + \dot{\boldsymbol{X}}^{\mathrm{T}}\left(\sum_j m_j\boldsymbol{A}_j^{\mathrm{T}}\boldsymbol{D}_j\right)\boldsymbol{\omega}_i \\
&\quad + \dot{\boldsymbol{X}}^{\mathrm{T}}\left(\sum_j m_j\boldsymbol{A}_j^{\mathrm{T}}\tilde{\boldsymbol{r}}_j^{\mathrm{T}}\right)\boldsymbol{\omega}_j + \dot{\boldsymbol{X}}^{\mathrm{T}}\left(\sum_j m_j\boldsymbol{A}_j^{\mathrm{T}}\boldsymbol{\Phi}_{j\mathrm{t}}\right)\dot{\boldsymbol{\eta}}_j \\
&\quad + \frac{1}{2}\boldsymbol{\omega}_{\mathrm{s}}^{\mathrm{T}}\left(\sum_j m_j\boldsymbol{B}_j^{\mathrm{T}}\boldsymbol{B}_j\right)\boldsymbol{\omega}_{\mathrm{s}} + \boldsymbol{\omega}_{\mathrm{s}}^{\mathrm{T}}\left(\sum_j m_j\boldsymbol{B}_j^{\mathrm{T}}\boldsymbol{D}_j\right)\boldsymbol{\omega}_i \\
&\quad + \boldsymbol{\omega}_{\mathrm{s}}^{\mathrm{T}}\left(\sum_j m_j\boldsymbol{B}_j^{\mathrm{T}}\tilde{\boldsymbol{r}}_j^{\mathrm{T}}\right)\boldsymbol{\omega}_j + \boldsymbol{\omega}_{\mathrm{s}}^{\mathrm{T}}\left(\sum_j m_j\boldsymbol{B}_j^{\mathrm{T}}\boldsymbol{\Phi}_{j\mathrm{t}}\right)\dot{\boldsymbol{\eta}}_j \\
&\quad + \boldsymbol{\omega}_{\mathrm{s}}^{\mathrm{T}}\left(\sum_j m_j\boldsymbol{B}_j^{\mathrm{T}}\boldsymbol{\Psi}_{j\mathrm{t}}\right)\boldsymbol{Q}_i^j\boldsymbol{\Phi}_{i*}\dot{\boldsymbol{\eta}}_i \\
&\quad + \frac{1}{2}\boldsymbol{\omega}_i^{\mathrm{T}}\left(\sum_j m_j\boldsymbol{D}_j^{\mathrm{T}}\boldsymbol{D}_j\right)\boldsymbol{\omega}_i + \boldsymbol{\omega}_i^{\mathrm{T}}\left(\sum_j m_j\boldsymbol{D}_j^{\mathrm{T}}\tilde{\boldsymbol{r}}_j^{\mathrm{T}}\right)\boldsymbol{\omega}_j \\
&\quad + \boldsymbol{\omega}_i^{\mathrm{T}}\left(\sum_j m_j\boldsymbol{D}_j^{\mathrm{T}}\boldsymbol{\Phi}_{j\mathrm{t}}\right)\dot{\boldsymbol{\eta}}_j + \boldsymbol{\omega}_i^{\mathrm{T}}\left(\sum_j m_j\boldsymbol{D}_j^{\mathrm{T}}\boldsymbol{\Psi}_{j\mathrm{t}}\right)\boldsymbol{Q}_i^j\boldsymbol{\Phi}_{i^*}\dot{\boldsymbol{\eta}}_i \\
&\quad + \frac{1}{2}\boldsymbol{\omega}_j^{\mathrm{T}}\left(\sum_j m_j\tilde{\boldsymbol{r}}_j\tilde{\boldsymbol{r}}_j^{\mathrm{T}}\right)\boldsymbol{\omega}_j + \boldsymbol{\omega}_j^{\mathrm{T}}\left(\sum_j m_j\tilde{\boldsymbol{r}}_j\boldsymbol{\Phi}_{j\mathrm{t}}\right)\dot{\boldsymbol{\eta}}_j \\
&\quad + \boldsymbol{\omega}_j^{\mathrm{T}}\left(\sum_j m_j\tilde{\boldsymbol{r}}_j\boldsymbol{\Psi}_{j\mathrm{t}}\right)\boldsymbol{Q}_i^j\boldsymbol{\Phi}_{i^*}\dot{\boldsymbol{\eta}}_i \\
&\quad + \frac{1}{2}\dot{\boldsymbol{\eta}}_j^{\mathrm{T}}\left(\sum_j m_j\boldsymbol{\Phi}_{j\mathrm{t}}^{\mathrm{T}}\boldsymbol{\Phi}_{j\mathrm{t}}\right)\boldsymbol{\eta}_j + \dot{\boldsymbol{\eta}}_j^{\mathrm{T}}\left(\sum_j m_j\boldsymbol{\Phi}_{j\mathrm{t}}^{\mathrm{T}}\boldsymbol{\Psi}_{j\mathrm{t}}\right)\boldsymbol{Q}_i^j\boldsymbol{\Phi}_{i^*}\dot{\boldsymbol{\eta}}_i \\
&\quad + \frac{1}{2}\dot{\boldsymbol{\eta}}_i^{\mathrm{T}}\boldsymbol{\Phi}_{i^*}^{\mathrm{T}}\boldsymbol{Q}_i^j\left(\sum_j m_j\boldsymbol{\Psi}_{j\mathrm{t}}^{\mathrm{T}}\boldsymbol{\Psi}_{j\mathrm{t}}\right)\boldsymbol{Q}_i^j\boldsymbol{\Phi}_{i^*}\dot{\boldsymbol{\eta}}_i \\
&\quad + \dot{\boldsymbol{X}}^{\mathrm{T}}\left(\sum_j m_j\boldsymbol{A}_j^{\mathrm{T}}\boldsymbol{\Psi}_{j\mathrm{t}}\right)\boldsymbol{Q}_i^j\boldsymbol{\Phi}_{i^*}\dot{\boldsymbol{\eta}}_i
\end{aligned} \tag{38}$$

where M_j is the mass of the second-stage flexible appendage j and m_j is the mass of the specified point. The second-stage flexible appendage j also has its elastic potential energy, which is

$$V_j = \frac{1}{2}\boldsymbol{\eta}_j^{\mathrm{T}}\boldsymbol{\Phi}_j^{\mathrm{T}}\boldsymbol{K}_{\mathrm{nn}}^{j}\boldsymbol{\Phi}_j\boldsymbol{\eta}_j = \frac{1}{2}\boldsymbol{\eta}_j^{\mathrm{T}}\boldsymbol{\Lambda}_j\boldsymbol{\eta}_j \tag{39}$$

where $\boldsymbol{K}_{\mathrm{nn}}^{j}$ is the stiffness matrix of the second-stage flexible appendage j, and $\boldsymbol{\Phi}_j$ and $\boldsymbol{\Lambda}_j$ are the normal mode matrix and the eigenvalue matrix under constrained boundary condition, respectively.

With the above derivations based on the substructure method and the hybrid coordinates, the system's kinetic energy and potential energy have been obtained. Using the Lagrange equation, the composite flexible dynamic model for the arm deploying phase can be obtained as follows:

$$M\ddot{\boldsymbol{X}} + \boldsymbol{P}_{\mathrm{s}}\dot{\boldsymbol{\omega}}_{\mathrm{s}} + \boldsymbol{P}_i\dot{\boldsymbol{\omega}}_i + \boldsymbol{P}_j\dot{\boldsymbol{\omega}}_j + \boldsymbol{F}_{\mathrm{t}i}\ddot{\boldsymbol{\eta}}_i + \boldsymbol{F}_{\mathrm{t}j}\ddot{\boldsymbol{\eta}}_j = \boldsymbol{F} \tag{40}$$

$$\boldsymbol{P}_{\mathrm{s}}^{\mathrm{T}}\ddot{\boldsymbol{X}} + \boldsymbol{I}_{\mathrm{s}}\dot{\boldsymbol{\omega}}_{\mathrm{s}} + \boldsymbol{R}_{\mathrm{s}i}\dot{\boldsymbol{\omega}}_i + \boldsymbol{R}_{\mathrm{s}j}\dot{\boldsymbol{\omega}}_j + \boldsymbol{F}_{\mathrm{s}i}\ddot{\boldsymbol{\eta}}_i + \boldsymbol{F}_{\mathrm{s}j}\ddot{\boldsymbol{\eta}}_j = \boldsymbol{M}_{b\mathrm{t}} \tag{41}$$

$$\boldsymbol{P}_i^{\mathrm{T}}\ddot{\boldsymbol{X}} + \boldsymbol{R}_{\mathrm{s}i}^{\mathrm{T}}\dot{\boldsymbol{\omega}}_{\mathrm{s}} + \boldsymbol{I}_i\dot{\boldsymbol{\omega}}_i + \boldsymbol{R}_{ij}\dot{\boldsymbol{\omega}}_j + \boldsymbol{F}_{ii}\ddot{\boldsymbol{\eta}}_i + \boldsymbol{F}_{ij}\ddot{\boldsymbol{\eta}}_j = \boldsymbol{M}_{i\mathrm{t}} \tag{42}$$

$$\boldsymbol{P}_j^{\mathrm{T}}\ddot{\boldsymbol{X}} + \boldsymbol{R}_{\mathrm{s}j}^{\mathrm{T}}\dot{\boldsymbol{\omega}}_{\mathrm{s}} + \boldsymbol{R}_{ij}^{\mathrm{T}}\dot{\boldsymbol{\omega}}_i + \boldsymbol{I}_j\dot{\boldsymbol{\omega}}_j + \boldsymbol{F}_{jj}\ddot{\boldsymbol{\eta}}_j + \boldsymbol{F}_{ji}\ddot{\boldsymbol{\eta}}_i = \boldsymbol{M}_{j\mathrm{t}} \tag{43}$$

$$\boldsymbol{F}_{\mathrm{t}i}^{\mathrm{T}}\ddot{\boldsymbol{X}} + \boldsymbol{F}_{\mathrm{s}i}^{\mathrm{T}}\dot{\boldsymbol{\omega}}_{\mathrm{s}} + \boldsymbol{F}_{ii}^{\mathrm{T}}\dot{\boldsymbol{\omega}}_i + \boldsymbol{F}_{ji}^{\mathrm{T}}\dot{\boldsymbol{\omega}}_j + \boldsymbol{V}_{ji}^{\mathrm{T}}\ddot{\boldsymbol{\eta}}_j + \boldsymbol{V}_{ii}\ddot{\boldsymbol{\eta}}_i + \boldsymbol{\Lambda}_i\boldsymbol{\eta}_i = \boldsymbol{0} \tag{44}$$

$$\boldsymbol{F}_{\mathrm{t}j}^{\mathrm{T}}\ddot{\boldsymbol{X}} + \boldsymbol{F}_{\mathrm{s}j}^{\mathrm{T}}\dot{\boldsymbol{\omega}}_{\mathrm{s}} + \boldsymbol{F}_{ij}^{\mathrm{T}}\dot{\boldsymbol{\omega}}_i + \boldsymbol{F}_{jj}^{\mathrm{T}}\dot{\boldsymbol{\omega}}_j + \ddot{\boldsymbol{\eta}}_j + \boldsymbol{V}_i\ddot{\boldsymbol{\eta}}_i + \boldsymbol{\Lambda}_i\boldsymbol{\eta}_i = \boldsymbol{0} \tag{45}$$

where

$$M = M_b + M_i + M_j,\ \boldsymbol{P}_j = \sum_j m_j\boldsymbol{A}_j^{\mathrm{T}}\tilde{\boldsymbol{r}}_j^{\mathrm{T}}$$

$$\boldsymbol{P}_{\mathrm{s}} = \sum_b m_b\boldsymbol{C}_o^{b\mathrm{T}}\tilde{\boldsymbol{r}}_b^{\mathrm{T}} + \sum_i m_i\boldsymbol{A}_i^{\mathrm{T}}\boldsymbol{B}_i + \sum_j m_j\boldsymbol{A}_j^{\mathrm{T}}\boldsymbol{B}_j$$

$$\boldsymbol{P}_i = \sum_i m_i\boldsymbol{A}_i^{\mathrm{T}}\tilde{\boldsymbol{r}}_i^{\mathrm{T}} + \sum_j m_j\boldsymbol{A}_j^{\mathrm{T}}\boldsymbol{D}_j$$

$$\boldsymbol{F}_{\mathrm{t}i} = \sum_i m_i\boldsymbol{A}_i^{\mathrm{T}}\boldsymbol{\Phi}_{i\mathrm{t}} + \sum_j m_j\boldsymbol{A}_j^{\mathrm{T}}\boldsymbol{\Psi}_{j\mathrm{t}}\boldsymbol{Q}_i^{j}\boldsymbol{\Phi}_{i^*},\ \boldsymbol{F}_{\mathrm{t}j} = \sum_j m_j\boldsymbol{A}_j^{\mathrm{T}}\boldsymbol{\Phi}_{j\mathrm{t}}$$

$$\boldsymbol{I}_{\mathrm{s}} = \sum_b m_b\tilde{\boldsymbol{r}}_b\tilde{\boldsymbol{r}}_b^{\mathrm{T}} + \sum_i m_i\boldsymbol{B}_i^{\mathrm{T}}\boldsymbol{B}_i + \sum_j m_j\boldsymbol{B}_j^{\mathrm{T}}\boldsymbol{B}_j$$

$$\boldsymbol{R}_{\mathrm{s}i} = \sum_i m_i\boldsymbol{B}_i^{\mathrm{T}}\tilde{\boldsymbol{r}}_i^{\mathrm{T}} + \sum_j m_j\boldsymbol{B}_j^{\mathrm{T}}\boldsymbol{D}_j,\ \boldsymbol{R}_{\mathrm{s}j} = \sum_j m_j\boldsymbol{B}_j^{\mathrm{T}}\tilde{\boldsymbol{r}}_j^{\mathrm{T}}$$

$$\boldsymbol{F}_{\mathrm{s}i} = \sum_i m_i\boldsymbol{B}_i^{\mathrm{T}}\boldsymbol{\Phi}_{i\mathrm{t}} + \sum_j m_j\boldsymbol{B}_j^{\mathrm{T}}\boldsymbol{\Psi}_{j\mathrm{t}}\boldsymbol{Q}_i^{j}\boldsymbol{\Phi}_{i^*},\ \boldsymbol{F}_{\mathrm{s}j} = \sum_j m_j\boldsymbol{B}_j^{\mathrm{T}}\boldsymbol{\Phi}_{j\mathrm{t}}$$

$$\boldsymbol{I}_i = \sum_i m_i\tilde{\boldsymbol{r}}_i\tilde{\boldsymbol{r}}_i^{\mathrm{T}} + \sum_j m_j\boldsymbol{D}_j^{\mathrm{T}}\boldsymbol{D}_j,\ \boldsymbol{R}_{ij} = \sum_j m_j\boldsymbol{D}_j^{\mathrm{T}}\tilde{\boldsymbol{r}}_j^{\mathrm{T}}$$

$$\boldsymbol{F}_{ii} = \sum_i m_i\tilde{\boldsymbol{r}}_i\boldsymbol{\Phi}_{i\mathrm{t}} + \sum_j m_j\boldsymbol{D}_j^{\mathrm{T}}\boldsymbol{\Psi}_{j\mathrm{t}}\boldsymbol{Q}_i^{j}\boldsymbol{\Phi}_{i^*},\ \boldsymbol{F}_{ij} = \sum_j m_j\boldsymbol{D}_j^{\mathrm{T}}\boldsymbol{\Phi}_{j\mathrm{t}}$$

$$\boldsymbol{I}_j = \sum_j m_j\tilde{\boldsymbol{r}}_j\tilde{\boldsymbol{r}}_j^{\mathrm{T}},\ \boldsymbol{F}_{jj} = \sum_j m_j\tilde{\boldsymbol{r}}_j\boldsymbol{\Phi}_{j\mathrm{t}},\ \boldsymbol{F}_{ji} = \sum_j m_j\tilde{\boldsymbol{r}}_j\boldsymbol{\Psi}_{j\mathrm{t}}\boldsymbol{Q}_i^{j}\boldsymbol{\Phi}_{i^*}$$

$$\boldsymbol{V}_{ji} = \sum_j m_j\boldsymbol{\Phi}_{j\mathrm{t}}^{\mathrm{T}}\boldsymbol{\Psi}_{j\mathrm{t}}\boldsymbol{Q}_i^{j}\boldsymbol{\Phi}_{i^*},\ \boldsymbol{V}_{ii} = \boldsymbol{I} + \boldsymbol{\Phi}_{i^*}^{\mathrm{T}}\boldsymbol{Q}_i^{j\mathrm{T}}\left(\sum_j m_j\boldsymbol{\Psi}_{j\mathrm{t}}^{\mathrm{T}}\boldsymbol{\Psi}_{j\mathrm{t}}\right)\boldsymbol{Q}_i^{j}\boldsymbol{\Phi}_{i^*}$$

$\boldsymbol{F}$ is the total external force of the satellite, $\boldsymbol{M}_{b\mathrm{t}}$ is the total external torque of the satellite bus b, $\boldsymbol{M}_{i\mathrm{t}}$ is the total external torque of the first-stage flexible appendage i, $\boldsymbol{M}_{j\mathrm{t}}$ is the total external torque of the second-stage flexible appendage j, and $\boldsymbol{I}$ is the identity matrix.

In the deploying process of a large deployable antenna, the total external force and the external torque are relatively small, so as the angular velocity of the flexible appendages. Therefore, some small variables such as $\ddot{\boldsymbol{X}}$, $\boldsymbol{F}$, $\boldsymbol{\omega}_i$, $\boldsymbol{\omega}_j$, $\boldsymbol{M}_{i\mathrm{t}}$, and $\boldsymbol{M}_{j\mathrm{t}}$ can be omitted. In this way, the composite flexible dynamic model can be further simplified as

$$\begin{bmatrix} \boldsymbol{I}_{\mathrm{s}} & \boldsymbol{F}_{\mathrm{s}i} & \boldsymbol{F}_{\mathrm{s}j} \\ \boldsymbol{F}_{\mathrm{s}i}^{\mathrm{T}} & \boldsymbol{V}_{ii} & \boldsymbol{V}_{ji}^{\mathrm{T}} \\ \boldsymbol{F}_{\mathrm{s}j}^{\mathrm{T}} & \boldsymbol{V}_{ji} & \boldsymbol{I} \end{bmatrix}\begin{bmatrix} \dot{\boldsymbol{\omega}}_{\mathrm{s}} \\ \ddot{\boldsymbol{\eta}}_i \\ \ddot{\boldsymbol{\eta}}_j \end{bmatrix} + \begin{bmatrix} \boldsymbol{0} & & \\ & \boldsymbol{\Lambda}_i & \\ & & \boldsymbol{\Lambda}_j \end{bmatrix}\begin{bmatrix} \boldsymbol{\omega}_{\mathrm{s}} \\ \boldsymbol{\eta}_i \\ \boldsymbol{\eta}_j \end{bmatrix} = \begin{bmatrix} \boldsymbol{M}_{b\mathrm{t}} \\ \boldsymbol{0} \\ \boldsymbol{0} \end{bmatrix} \tag{46}$$

Utilizing the effective inertia matrix truncation criterion, the number of modes included in the model of Eq. (46) can be selected according to specified requirements.

To validate the composite flexible dynamic model for the arm deploying phase, an example is made as shown in Fig. 6. In this example, the structural frequencies are calculated according to the composite flexible dynamic model (Eq. (46)) and the classical hybrid coordinate model, with the results compared in Table 2. In the composite flexible dynamic model, the mass matrix and the stiffness matrix are

$$\boldsymbol{M}_{\mathrm{arm}} = \begin{bmatrix} \boldsymbol{V}_{ii} & \boldsymbol{V}_{ji}^{\mathrm{T}} \\ \boldsymbol{V}_{ji} & \boldsymbol{I} \end{bmatrix} \tag{47}$$

$$\boldsymbol{K}_{\mathrm{arm}} = \begin{bmatrix} \boldsymbol{\Lambda}_i & \\ & \boldsymbol{\Lambda}_j \end{bmatrix} \tag{48}$$

2.4. Flexible dynamic modeling for the reflector deploying phase

In the reflector deploying phase, it is difficult to establish a practically applicable low-order dynamic model because there are hundreds of movable parts in the reflector, and the configuration is uncertain during the reflector deploying. To solve such problems, we take the modeling strategy of only building

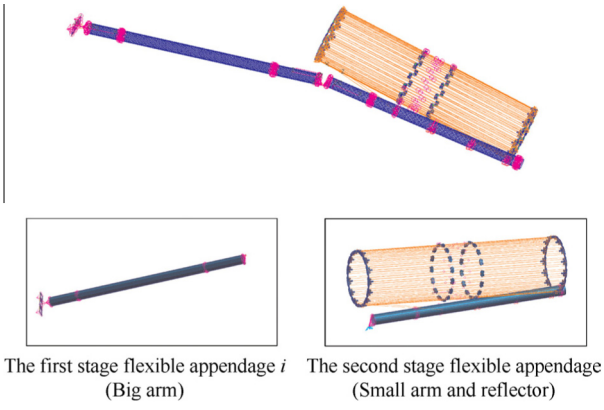

Fig. 6 A validation example of the composite flexible model.

Table 2 Validation results of the composite flexible dynamic model.

Model	The 1st modal frequency (Hz)	The 2nd modal frequency (Hz)	The 3rd modal frequency (Hz)
Composite flexible model	0.4448	0.4691	1.2112
Hybrid coordinate model	0.4446	0.4688	1.2101
Relative error (%)	0.04	0.06	0.09

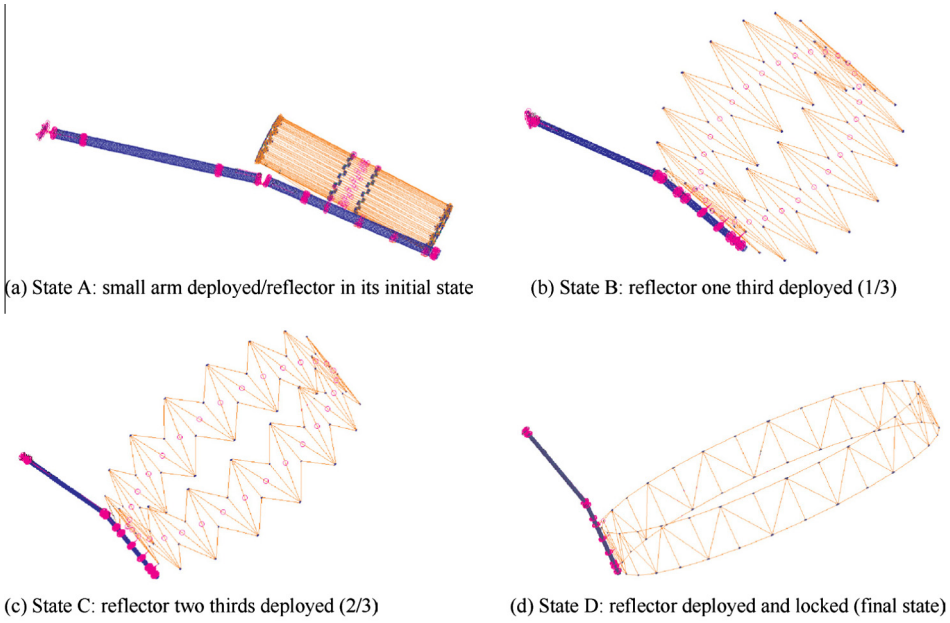

Fig. 7 Finite element models for the four typical deploying states.

dynamic models for typical deploying states of the reflector. In this paper, four states are modeled to approximately characterize the reflector deploying process, as shown in Fig. 7.

The inertia tensors, the structural frequencies, and the rotational coupling coefficients of these typical deploying states are calculated with the built hybrid coordinate flexible dynamic model. Results of the calculation are given in the Appendix A.

3. Attitude control for the deploying process

Considering the dynamic features of a satellite with a large deployable antenna, major requirements on the attitude control design include the following:

(1) The closed-loop system stability should be independent of the inertia tensor, the structural frequencies, and the rotational coupling coefficients, for the fact that these dynamic parameters change widely and are difficult to be accurately estimated.
(2) The attitude control system should be designed with multi-input multi-output (MIMO) approaches owing to the notable coupling among the roll/pitch/yaw axis.
(3) The control method should have good disturbance rejection capability for keeping attitude stability under deploying disturbances such as locking/unlocking impact.

To satisfy above requirements, in this section, a robust control method is proposed. Then the H_∞ performance index optimization is performed to optimize the disturbance rejection capability, which yields a robust attitude control with good disturbance rejection performance.

3.1. Robust control design

Let $\cdot(v)$ denote the variable dynamic parameters during the deploying process, and subscripts "s", "n", and "a" denote the south solar array, the north solar array, and the flexible antenna, respectively (the satellite is shown in Fig. 1(e)). The hybrid coordinate dynamic equations can be written as

$$\boldsymbol{I}_{\mathrm{s}}(v)\ddot{\boldsymbol{\theta}} + \boldsymbol{F}_{\mathrm{s,s}}\ddot{\boldsymbol{\eta}}_{\mathrm{s}} + \boldsymbol{F}_{\mathrm{s,n}}\ddot{\boldsymbol{\eta}}_{\mathrm{n}} + \boldsymbol{F}_{\mathrm{s,a}}(v)\ddot{\boldsymbol{\eta}}_{\mathrm{a}} = \boldsymbol{u} + \boldsymbol{w} \tag{49}$$

$$\ddot{\boldsymbol{\eta}}_{\mathrm{s}} + 2\zeta_{\mathrm{s}}\boldsymbol{\Omega}_{\mathrm{s}}\dot{\boldsymbol{\eta}}_{\mathrm{s}} + \boldsymbol{\Omega}_{\mathrm{s}}^2\boldsymbol{\eta}_{\mathrm{s}} + \boldsymbol{F}_{\mathrm{s,s}}^{\mathrm{T}}\ddot{\boldsymbol{\theta}} = \boldsymbol{0} \tag{50}$$

$$\ddot{\boldsymbol{\eta}}_{\mathrm{n}} + 2\zeta_{\mathrm{n}}\boldsymbol{\Omega}_{\mathrm{n}}\dot{\boldsymbol{\eta}}_{\mathrm{n}} + \boldsymbol{\Omega}_{\mathrm{n}}^2\boldsymbol{\eta}_{\mathrm{n}} + \boldsymbol{F}_{\mathrm{s,n}}^{\mathrm{T}}\ddot{\boldsymbol{\theta}} = \boldsymbol{0} \tag{51}$$

$$\ddot{\boldsymbol{\eta}}_{\mathrm{a}} + 2\zeta_{\mathrm{a}}(v)\boldsymbol{\Omega}_{\mathrm{a}}(v)\dot{\boldsymbol{\eta}}_{\mathrm{a}} + \boldsymbol{\Omega}_{\mathrm{a}}^2(v)\boldsymbol{\eta}_{\mathrm{a}} + \boldsymbol{F}_{\mathrm{s,a}}^{\mathrm{T}}(v)\ddot{\boldsymbol{\theta}} = \boldsymbol{0} \tag{52}$$

where $\boldsymbol{\theta}$, $\boldsymbol{I}_{\mathrm{s}}(v)$, $\boldsymbol{F}_{\mathrm{s}}$, $\boldsymbol{u}$, and $\boldsymbol{w}$ are the satellite attitude vector, the inertia tensor of the whole satellite, the rotational coupling coefficients, the control torque, and the disturbance torque. Definitions for the modal parameters are the modal coordinate vector $\boldsymbol{\eta}$, the modal damping matrix $\boldsymbol{\zeta}$, and the modal frequency matrix $\boldsymbol{\Omega}$. The output of this model is

$$\boldsymbol{y} = \begin{bmatrix}\boldsymbol{\theta}^{\mathrm{T}} & \dot{\boldsymbol{\theta}}^{\mathrm{T}}\end{bmatrix}^{\mathrm{T}} \tag{53}$$

By defining a vector $\boldsymbol{x} = \begin{bmatrix}\boldsymbol{\theta}^{\mathrm{T}} & \boldsymbol{\eta}_{\mathrm{n}}^{\mathrm{T}} & \boldsymbol{\eta}_{\mathrm{s}}^{\mathrm{T}} & \boldsymbol{\eta}_{\mathrm{a}}^{\mathrm{T}}\end{bmatrix}^{\mathrm{T}}$, the dynamic model expressed by Eqs. (49)–(52) can be rewritten in a compact form as

$$\boldsymbol{M}(v)\ddot{\boldsymbol{x}} + \boldsymbol{C}(v)\dot{\boldsymbol{x}} + \boldsymbol{K}(v)\boldsymbol{x} = \boldsymbol{S}\boldsymbol{u} + \boldsymbol{S}\boldsymbol{w} \tag{54}$$

where

$$\boldsymbol{M}(v) = \begin{bmatrix} \boldsymbol{I}_{\mathrm{s}}(v) & \boldsymbol{F}_{\mathrm{s,n}} & \boldsymbol{F}_{\mathrm{s,s}} & \boldsymbol{F}_{\mathrm{s,a}}(v) \\ \boldsymbol{F}_{\mathrm{s,n}}^{\mathrm{T}} & \boldsymbol{I} & & \\ \boldsymbol{F}_{\mathrm{s,s}}^{\mathrm{T}} & & \boldsymbol{I} & \\ \boldsymbol{F}_{\mathrm{s,a}}^{\mathrm{T}}(v) & & & \boldsymbol{I} \end{bmatrix}$$

$$\boldsymbol{C}(v) = \mathrm{diag}(0, 2\zeta_{\mathrm{n}}\boldsymbol{\Omega}_n, 2\zeta_{\mathrm{s}}\boldsymbol{\Omega}_{\mathrm{s}}, 2\zeta_{\mathrm{a}}\boldsymbol{\Omega}_{\mathrm{a}}(v))$$

$$\boldsymbol{K}(v) = \mathrm{diag}(0, \boldsymbol{\Omega}_{\mathrm{n}}^2, \boldsymbol{\Omega}_{\mathrm{s}}^2, \boldsymbol{\Omega}_{\mathrm{a}}^2(v))$$

$$\boldsymbol{S} = \begin{bmatrix}\boldsymbol{I} & \boldsymbol{0} & \boldsymbol{0} & \boldsymbol{0}\end{bmatrix}^{\mathrm{T}}$$

Lemma 1. *If the parameters of Eq. (54) satisfy*

$$\boldsymbol{M}(v) > \boldsymbol{0},\ \boldsymbol{C}(\delta) \geqslant \boldsymbol{0},\ \boldsymbol{K}(\delta) \geqslant \boldsymbol{0}$$

then the system is detectable and stabilizable. [12]

If the location and velocity feedback

$$\boldsymbol{u} = -[\boldsymbol{G}_{\mathrm{l}} \quad \boldsymbol{G}_{\mathrm{v}}]\boldsymbol{y} \tag{55}$$

$$\boldsymbol{y} = [\boldsymbol{x}^{\mathrm{T}}\boldsymbol{S} \quad \dot{\boldsymbol{x}}^{\mathrm{T}}\boldsymbol{S}]^{\mathrm{T}} \tag{56}$$

satisfy

$$\boldsymbol{G}_{\mathrm{l}} > 0,\ \boldsymbol{G}_{\mathrm{v}} > \boldsymbol{0} \tag{57}$$

according to Eqs. (54)–(56), the closed-loop system can be given by

$$\boldsymbol{M}(v)\ddot{\boldsymbol{x}} + \boldsymbol{C}_{\mathrm{closed}}(v)\dot{\boldsymbol{x}} + \boldsymbol{K}_{\mathrm{closed}}(v)\boldsymbol{x} = \boldsymbol{S}\boldsymbol{w} \tag{58}$$

where $\boldsymbol{C}_{\mathrm{closed}}(v) = \boldsymbol{C}(v) + \boldsymbol{S}\boldsymbol{G}_{\mathrm{v}}\boldsymbol{S}^{\mathrm{T}}$ and $\boldsymbol{K}_{\mathrm{closed}}(v) = \boldsymbol{K}(v) + \boldsymbol{S}\boldsymbol{G}_{\mathrm{l}}\boldsymbol{S}^{\mathrm{T}}$.

Lemma 2. *If the system defined by Eqs. (53) and (54) is detectable and stabilizable, then the closed-loop system (58) satisfies* [12]:

$$\boldsymbol{C}_{\mathrm{closed}}(v) > 0, \boldsymbol{K}_{\mathrm{closed}}(v) > \boldsymbol{0} \tag{59}$$

Lemma 3. *(Schur Complementary): For a given symmetric matrix* $\boldsymbol{R} = \begin{bmatrix} \boldsymbol{R}_{11} & \boldsymbol{R}_{12} \\ \boldsymbol{R}_{21} & \boldsymbol{R}_{22} \end{bmatrix} > \boldsymbol{0}$, *the following propositions are equivalent:*

(1) $\boldsymbol{R} > \boldsymbol{0}$
(2) $\boldsymbol{R}_{11} > \boldsymbol{0},\ \boldsymbol{R}_{22} - \boldsymbol{R}_{12}^{\mathrm{T}}\boldsymbol{R}_{11}^{-1}\boldsymbol{R}_{12} > \boldsymbol{0}$
(3) $\boldsymbol{R}_{22} > \boldsymbol{0},\ \boldsymbol{R}_{11} - \boldsymbol{R}_{21}^{\mathrm{T}}\boldsymbol{R}_{22}^{-1}\boldsymbol{R}_{21} > \boldsymbol{0}$

By generalizing the theorem proposed in Ref.,[12] we can arrive at Theorem 1.

Theorem 1. *In the deploying process of a large deployable antenna, for any* $\boldsymbol{M}(v)$, $\boldsymbol{C}_{\mathrm{closed}}(v)$, *and* $\boldsymbol{K}_{\mathrm{closed}}(v)$, *the closed-loop system defined by Eq. (58) keeps stable.*

Proof. According to Lemmas 1 and 2, for any $\boldsymbol{M}(v)$, $\boldsymbol{C}_{\mathrm{closed}}(v)$, and $\boldsymbol{K}_{\mathrm{closed}}(v)$, there is

$$\boldsymbol{M}(v) > \boldsymbol{0},\ \boldsymbol{C}_{\mathrm{closed}}(v) > \boldsymbol{0},\ \boldsymbol{K}_{\mathrm{closed}}(v) > \boldsymbol{0} \tag{60}$$

Let $\boldsymbol{X}^{\mathrm{T}} = [\boldsymbol{x}^{\mathrm{T}} \quad \dot{\boldsymbol{x}}^{\mathrm{T}}]$, then the closed-loop system can be rewritten as

$$\dot{\boldsymbol{X}} = \boldsymbol{A}(v)\boldsymbol{X} + \boldsymbol{B}(v)\boldsymbol{w} \tag{61}$$

where

$$\begin{cases} \boldsymbol{A}(v) = \begin{bmatrix} \boldsymbol{0} & \boldsymbol{I} \\ -\boldsymbol{M}^{-1}(v)\boldsymbol{K}_{\mathrm{closed}}(v) & -\boldsymbol{M}^{-1}(v)\boldsymbol{C}_{\mathrm{closed}}(v) \end{bmatrix} \\ \boldsymbol{B}(v) = \begin{bmatrix} \boldsymbol{0} \\ \boldsymbol{M}^{-1}(v)\boldsymbol{L} \end{bmatrix} \end{cases} \tag{62}$$

The necessary and sufficient condition for the system (61) stability is that there is a symmetric matrix $\boldsymbol{P} > \boldsymbol{0}$, which satisfies the following Lyapunov inequality

$$\boldsymbol{P}\boldsymbol{A}(v) + \boldsymbol{A}^{\mathrm{T}}(v)\boldsymbol{P} < \boldsymbol{0} \tag{63}$$

Suppose that $\boldsymbol{P}_{\boldsymbol{0}} = \begin{bmatrix} \boldsymbol{K}_{\mathrm{closed}}(v) & \beta\boldsymbol{M}(v) \\ \beta\boldsymbol{M}(v) & \boldsymbol{M}(v) \end{bmatrix}$ and note that $\boldsymbol{K}_{\mathrm{closed}}(v) > \boldsymbol{0}$ and $\boldsymbol{M}(v) > \boldsymbol{0}$, so that $\forall \boldsymbol{P} \neq \boldsymbol{0}$ yielding

$$\boldsymbol{P}^{\mathrm{T}}\boldsymbol{K}_{\mathrm{closed}}(v)\boldsymbol{P} = \delta_{\boldsymbol{K}}(\boldsymbol{P}) > 0 \tag{64}$$

$$\boldsymbol{P}^{\mathrm{T}}\boldsymbol{M}(v)\boldsymbol{P} = \delta_{\boldsymbol{M}}(\boldsymbol{P}) > 0 \tag{65}$$

Therefore, $\exists 0 < \beta < \beta_1 = \sqrt{\dfrac{\delta_{\boldsymbol{K}}(\boldsymbol{P})}{\delta_{\boldsymbol{M}}(\boldsymbol{P})}}$, making $\boldsymbol{P}^{\mathrm{T}}\boldsymbol{K}_{\mathrm{closed}}(v)\boldsymbol{P} - \beta^2\boldsymbol{P}^{\mathrm{T}}\boldsymbol{M}(v)\boldsymbol{P} > \boldsymbol{0}$, i.e.,

$$\boldsymbol{K}_{\mathrm{closed}}(v) - \beta^2\boldsymbol{M}(v) > \boldsymbol{0} \tag{66}$$

According to Lemma 3, we can obtain that $\boldsymbol{P}_0 > \boldsymbol{0}$, and

$$\boldsymbol{P}_0\boldsymbol{A}(v) + \boldsymbol{A}^{\mathrm{T}}(v)\boldsymbol{P}_0 = -\boldsymbol{Q}(v) \tag{67}$$

where $\boldsymbol{Q}(v) = \begin{bmatrix} 2\beta\boldsymbol{K}_{\mathrm{closed}}(v) & \beta\boldsymbol{C}_{\mathrm{closed}}(v) \\ \beta\boldsymbol{C}_{\mathrm{closed}}(v) & 2\boldsymbol{C}_{\mathrm{closed}}(v) - 2\beta\boldsymbol{M}(v) \end{bmatrix}$.

Because $\boldsymbol{K}_{\mathrm{closed}}(v) > \boldsymbol{0}$, $\boldsymbol{C}_{\mathrm{closed}}(v) > \boldsymbol{0}$, and $\boldsymbol{M}(v) > \boldsymbol{0}$, $\forall \boldsymbol{P} \neq \boldsymbol{0}$, there is

$$2\boldsymbol{P}^{\mathrm{T}}\boldsymbol{C}_{\mathrm{closed}}(v)\boldsymbol{P} = \delta_{\boldsymbol{C}}(\boldsymbol{P}) > 0 \tag{68}$$

$$\boldsymbol{P}^{\mathrm{T}}\left(2\boldsymbol{M}(v) + \frac{\boldsymbol{C}_{\mathrm{closed}}\boldsymbol{K}_{\mathrm{closed}}^{-1}\boldsymbol{C}_{\mathrm{closed}}}{2}\right)\boldsymbol{P} = \delta(\boldsymbol{P}) > 0 \tag{69}$$

Hence, $\exists 0 < \beta < \beta_2 = \dfrac{\delta_{\boldsymbol{C}}(\boldsymbol{P})}{\delta(\boldsymbol{P})}$, making

$$2\boldsymbol{C}_{\mathrm{closed}} - \beta\left(2\boldsymbol{M}(v) + \frac{\boldsymbol{C}_{\mathrm{closed}}\boldsymbol{K}_{\mathrm{closed}}^{-1}\boldsymbol{C}_{\mathrm{closed}}}{2}\right) > \boldsymbol{0} \tag{70}$$

According to Lemma 3, we know that $\boldsymbol{Q}(v) > \boldsymbol{0}$.

Overall, when $0 < \beta < \min\{\beta_1, \beta_2\}$, $\exists \boldsymbol{P}_0 > \boldsymbol{0}$ (symmetric) satisfies the following Lyapunov inequality

$$\boldsymbol{P}_0\boldsymbol{A}(v) + \boldsymbol{A}^{\mathrm{T}}(v)\boldsymbol{P}_0 = -\boldsymbol{Q}(v) < \boldsymbol{0} \tag{71}$$

Therefore, in the deploying process of the antenna, the closed-loop system keeps stable under uncertain $\boldsymbol{M}(v)$, $\boldsymbol{C}_{\mathrm{closed}}(v)$, and $\boldsymbol{K}_{\mathrm{closed}}(v)$. □

3.2. H_∞ performance index optimization

According to the attitude control requirements of the antenna deploying process, good disturbance rejection performance is important to maintain the satellite attitude stable. Firstly, select the output $\boldsymbol{z}$ as

$$\boldsymbol{z} = \begin{bmatrix} \boldsymbol{\theta} \\ \eta\dot{\boldsymbol{\theta}} \end{bmatrix} \tag{72}$$

where η is the weight to balance the angle or the angle velocity design target. Taking the disturbance torque $\boldsymbol{w}$ as the external input and $\boldsymbol{z}$ as the output, the system's state equations can be given by

$$\dot{\boldsymbol{X}} = \boldsymbol{A}(v)\boldsymbol{X} + \boldsymbol{B}(v)\boldsymbol{w} \tag{73}$$

$$\boldsymbol{z} = \boldsymbol{C}\boldsymbol{X} \tag{74}$$

where

$$\boldsymbol{C} = \mathrm{diag}(\boldsymbol{S}^{\mathrm{T}}, \eta\boldsymbol{S}^{\mathrm{T}}) \tag{75}$$

According to the state Eqs. (73) and (74), the transfer function matrix from $\boldsymbol{w}$ to $\boldsymbol{z}$ can be expressed as

$$\boldsymbol{T}(s) = \boldsymbol{C}(s\boldsymbol{I} - \boldsymbol{A})^{-1}\boldsymbol{B} \tag{76}$$

and its H_∞ norm can be given by

$$\|\boldsymbol{T}(s)\|_\infty = \sup_{\omega} \sigma_{\max}(\boldsymbol{T}(\mathrm{j}\omega)) = \Gamma_{ee} = \sup_{\|\boldsymbol{w}\|_2 \leq 1} \|\boldsymbol{z}\|_2 \tag{77}$$

where $\sigma_{\max}(\boldsymbol{T}(j\omega))$ is the maximum singular value of the closed-loop frequency response, and Γ_{ee} is the energy to energy gain. By minimizing the H_∞ norm in Eq. (77), the disturbance rejection performance can also be enhanced. Lemma 4 is introduced to optimize the controller disturbance rejection.

Lemma 4. [29]: *Using the following optimizing calculation*

$$\min \gamma \tag{78}$$

$$\text{s.t.} \begin{bmatrix} \boldsymbol{A}^{\mathrm{T}}\boldsymbol{P}+\boldsymbol{P}\boldsymbol{A} & \boldsymbol{P}\boldsymbol{B} & \boldsymbol{C}^{\mathrm{T}} \\ \boldsymbol{B}^{\mathrm{T}}\boldsymbol{P} & -r\boldsymbol{I} & \boldsymbol{D}^{\mathrm{T}} \\ \boldsymbol{C} & \boldsymbol{D} & -r\boldsymbol{I} \end{bmatrix} < \boldsymbol{0} \tag{79}$$

$$\boldsymbol{P} > \boldsymbol{0} \tag{80}$$

The minimum H_∞ solution can be obtained.

Substituting $\boldsymbol{P}_0 = \begin{bmatrix} \boldsymbol{K}_{\text{closed}}(v) & \beta\boldsymbol{M}(v) \\ \beta\boldsymbol{M}(v) & \boldsymbol{M}(v) \end{bmatrix} > \boldsymbol{0}$ into Eq. (79) and according to Lemma 3 (Schur Complementary), Eq. (79) can be rewritten as

$$\begin{bmatrix} (\beta^2+1)\boldsymbol{S}\boldsymbol{S}^{\mathrm{T}} & \beta\boldsymbol{S}\boldsymbol{S}^{\mathrm{T}} \\ \beta\boldsymbol{S}\boldsymbol{S}^{\mathrm{T}} & (1+\eta^2)\boldsymbol{S}\boldsymbol{S}^{\mathrm{T}} \end{bmatrix} < \gamma\boldsymbol{Q}(v) \tag{81}$$

where

$$\boldsymbol{Q}(v) = \begin{bmatrix} 2\beta\boldsymbol{K}_{\text{closed}}(v) & \beta\boldsymbol{C}_{\text{closed}}(v) \\ \beta\boldsymbol{C}_{\text{closed}}(v) & 2\boldsymbol{C}_{\text{closed}}(v) - 2\beta\boldsymbol{M}(v) \end{bmatrix} \tag{82}$$

For any given dynamic model (58), the linear matrix inequality (LMI) solver of the MATLAB can be used to solve the LMI problem of Eq. (81), i.e., the controller $\boldsymbol{G} = [\boldsymbol{G}_{\mathrm{l}} \quad \boldsymbol{G}_{\mathrm{v}}]$ can be obtained which minimizes $\|\boldsymbol{T}(s)\|_\infty$. In a practical design, considering some engineering factors such as control authority limitation (induced by fly wheels), we can obtain the controller $\boldsymbol{G} = [\boldsymbol{G}_{\mathrm{l}} \quad \boldsymbol{G}_{\mathrm{v}}]$ which satisfies the sub-optimal index

$$\|\boldsymbol{T}(s)\|_\infty < \gamma_0. \tag{83}$$

3.3. Controller parameter design for the deploying process

In the deploying process, matrices $\boldsymbol{M}(v)$, $\boldsymbol{C}(v)$, and $\boldsymbol{K}(v)$ are time-varying due to the time-varying dynamic features, which make it infeasible to use the LMI approach. Via the convex decomposition, this time-varying dynamics can be expressed as

$$\boldsymbol{M}(v) = \sum_{l=1}^{n} \lambda_l \boldsymbol{M}_l \tag{84}$$

$$\boldsymbol{C}(v) = \sum_{l=1}^{n} \lambda_l \boldsymbol{C}_l \tag{85}$$

$$\boldsymbol{K}(v) = \sum_{l=1}^{n} \lambda_l \boldsymbol{K}_l \tag{86}$$

where n is the number of the typical states, λ_l is the weighting coefficient, and $\boldsymbol{M}_l$, $\boldsymbol{C}_l$, and $\boldsymbol{K}_l$ are the typical state parameters. In fact, these decompositions use the weighting sum of several typical states to approximately describe the dynamic features of any state in the deploying process. If the number of these typical states is large enough and these typical states properly distribute over the whole deploying stages, representing all the key deploying motions, these approximations can properly describe the dynamic features of the antenna deploying process. Then, with Eqs. (84)–(86), Eq. (81) can be rewritten as

$$\sum_{l=1}^{n} \lambda_l \left\{ \begin{bmatrix} (\beta^2+1)\boldsymbol{S}\boldsymbol{S}^{\mathrm{T}} & \beta\boldsymbol{S}\boldsymbol{S}^{\mathrm{T}} \\ \beta\boldsymbol{S}\boldsymbol{S}^{\mathrm{T}} & (1+\eta^2)\boldsymbol{S}\boldsymbol{S}^{\mathrm{T}} \end{bmatrix} - \gamma\boldsymbol{Q}_l(v) \right\} < \boldsymbol{0} \tag{87}$$

where

$$\boldsymbol{Q}_l = \begin{bmatrix} 2\beta(\boldsymbol{K}_l + \boldsymbol{S}\boldsymbol{G}_{\mathrm{l}}\boldsymbol{S}^{\mathrm{T}}) & \beta(\boldsymbol{C}_l + \boldsymbol{S}\boldsymbol{G}_{\mathrm{v}}\boldsymbol{S}^{\mathrm{T}}) \\ \beta(\boldsymbol{C}_l + \boldsymbol{S}\boldsymbol{G}_{\mathrm{v}}\boldsymbol{S}^{\mathrm{T}}) & 2(\boldsymbol{C}_l + \boldsymbol{S}\boldsymbol{G}_{\mathrm{v}}\boldsymbol{S}^{\mathrm{T}}) - 2\beta\boldsymbol{M}_l \end{bmatrix} \tag{88}$$

Then the optimization is turned into solving the following LMI problem:

$$\min \gamma \tag{89}$$

$$\text{s.t.} \begin{bmatrix} (\beta^2+1)\boldsymbol{S}\boldsymbol{S}^{\mathrm{T}} & \beta\boldsymbol{S}\boldsymbol{S}^{\mathrm{T}} \\ \beta\boldsymbol{S}\boldsymbol{S}^{\mathrm{T}} & (1+\eta^2)\boldsymbol{S}\boldsymbol{S}^{\mathrm{T}} \end{bmatrix} - \gamma\boldsymbol{Q}_l(v) < \boldsymbol{0} \; (l = 1,2,\ldots,n) \tag{90}$$

$$\boldsymbol{G}_{\mathrm{l}} > 0, \boldsymbol{G}_{\mathrm{v}} > \boldsymbol{0} \tag{91}$$

Clearly, it is difficult even impossible to establish $\boldsymbol{M}_l$, $\boldsymbol{C}_l$, and $\boldsymbol{K}_l$ for each state in the deploying process. Therefore, according to the aforementioned requirements to properly describe the deploying dynamic features, seven typical states are selected in all, including the four typical states shown in Fig. 7 and the other three shown in Fig. 8, with the corresponding descriptions and parameters listed in the Appendix A.

Taking $\beta = 0.0001$, $\eta = 48.5366$, and the sub-optimal target as 1 yields the following attitude controller

(a) State E: initial state (b) State F: big arm deployed (c) State G: big arm turned 90°

Fig. 8 Finite element models for the other three typical deploying states.

$$\boldsymbol{G}_{\mathrm{l}} = \mathrm{diag}(-294, -294, -294) \tag{92}$$

$$\boldsymbol{G}_{\mathrm{v}} = \mathrm{diag}(-882, -881, -882) \tag{93}$$

The design principle can be summarized as follows:

(1) Adjust η to change the overshoot and settling time of the attitude response.
(2) The main constraints of the optimization target is the torque limitation induced by fly wheels, and the smaller the H_∞ optimization target, the better the disturbance rejection capability, but the higher the torque limitation requirement.

4. Dynamics and control simulation of the deploying process

4.1. Whole deploying process simulation using the multi-rigid-body dynamic model

Using the multi-rigid-body dynamic model for the whole deploying process (proposed in Section 2.2) and the robust attitude controller (proposed in Section 3), the whole deploying process dynamics and control simulation can be performed. The roll, pitch and yaw angle responses during the deploying process are shown in Fig. 9.

From the simulation data, we can obtain the following results:

(1) In the whole deploying process, the variation range of the roll angle is in $\pm 0.05°$, and those of the pitch and yaw angles are $\pm 0.8°$ and $\pm 0.05°$, respectively. The stability and control authority requirements (< 1 N·m) are satisfied in the three directions, which indicates that the attitude control method proposed in this paper can maintain good performance under the condition of widely changing dynamic parameters.
(2) The simulation results show that the main disturbance in the deploying process is the reflector unlocking/locking procedure. Therefore, except for a proper attitude control design, an important factor for improving the attitude response during the deploying phase is to reduce the shocks generated by the unlocking/locking mechanism.

4.2. Deployable arm deploying phase simulation using the composite flexible dynamic model

Using the composite flexible dynamic model, the variations of the dynamic characteristics during the arm deploying phase can be obtained analytically. For example, the first three frequencies during the arm deploying phase are given in Fig. 10.

Similarly, the inertia tensor and the rotational coupling coefficients can be obtained using this composite flexible dynamic model. Then the dynamic and control simulation can be performed, results of which are shown in Fig. 11.

Simulation results shown in Figs. 11 indicate that, the closed-loop system stability can be ensured even when flexible dynamic parameters such as the structural frequencies and the rotational coupling coefficients change in wide ranges.

4.3. Reflector deploying phase simulation using the approximate dynamic model

In the reflector deploying phase, the flexible dynamic models of four typical states are built to approximately describe the

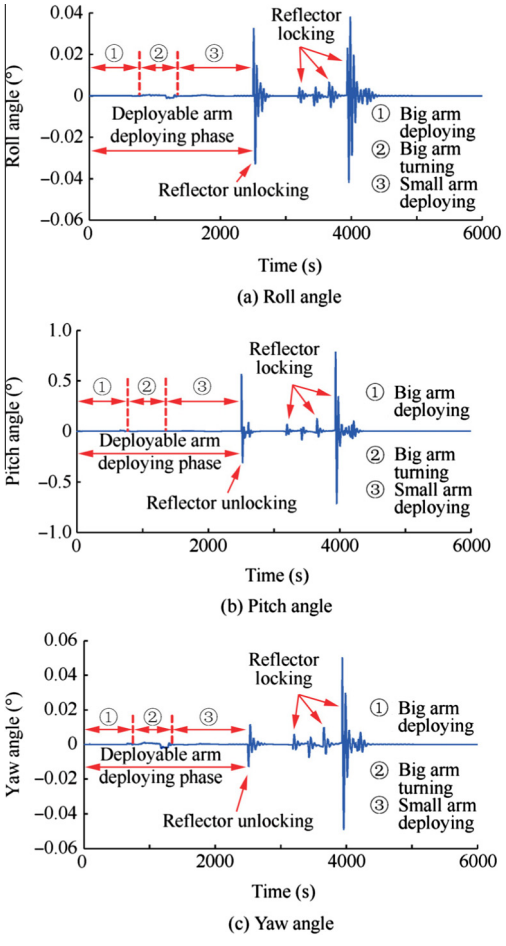

Fig. 9 Roll, pitch and yaw angle responses during the deploying process.

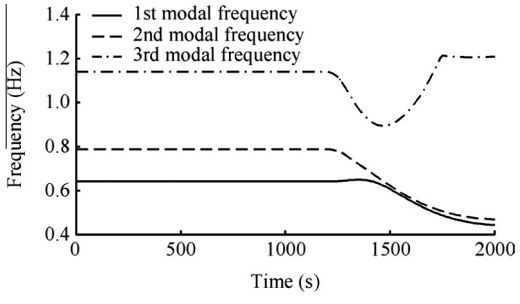

Fig. 10 The first three frequencies during the deployable arm deploying phase.

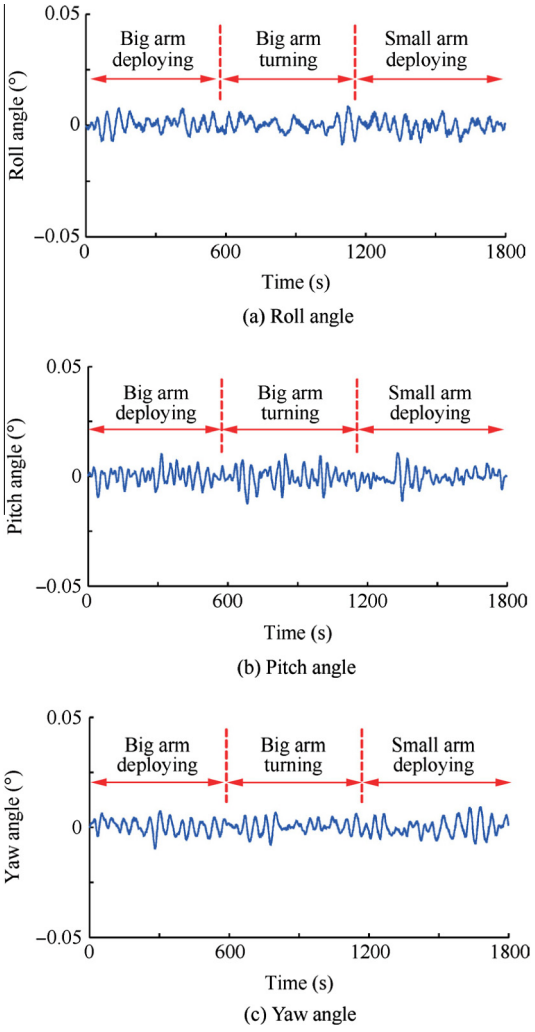

Fig. 11 Roll, pitch and yaw angle responses during the deployable arm deploying phase.

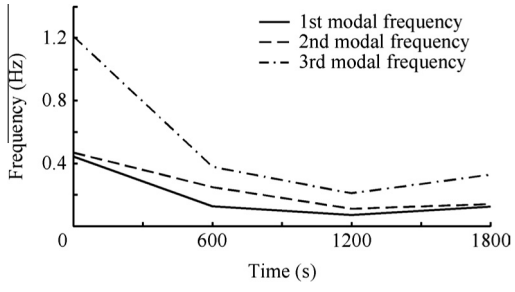

Fig. 12 The first three frequencies during the reflector deploying phase.

dynamics. With this approach, the variation trend of the dynamic parameters, for example the first three modal frequencies, can be obtained as shown in Fig. 12. The attitude control results for the reflector deploying phase are shown in Fig. 13.

These simulation results indicate that the attitude stability can also be ensured in the phase of reflector deploying, which

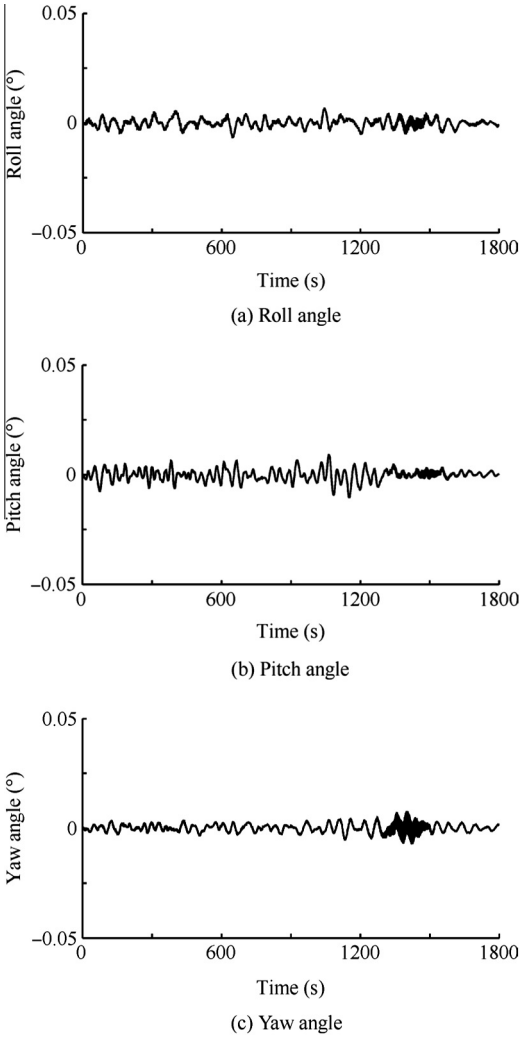

Fig. 13 Roll, pitch and yaw angle responses during the reflector deploying phase.

means that the design requirements are satisfied with the proposed controller in this paper.

5. Conclusions

(1) To describe a complicated antenna deploying process in a practically realizable and low-order approach, this paper develops three dynamic models. Among these models, a multi-rigid-body dynamic model is established to simulate the inertia tensor variation during the whole deploying process, and a composite flexible dynamic model for the deployable arm deploying phase is built to analytically describe the flexible structural parameters, while in the reflector deploying phase, a set of models are set up for several selected typical states to deal with the problem of time-varying structural parameters.

(2) An attitude control method is proposed in this paper, stability of which is independent of the time-varying structural parameters. In order to maintain the satellite attitude during the deploying process, the H_∞

optimization approach is taken to achieve better disturbance rejection performance, hence a robust attitude controller is obtained for the deploying process.

(3) A simplified cable dynamic model is developed. By inserting this model into the multi-body dynamic model built in the present paper, the unsynchronized phenomenon, which has been discovered in practical ground antenna deploying tests, can be rediscovered from computer simulation.

Acknowledgements

The authors thank Professor Bong Wie at Iowa State University, USA for his valuable discussions and suggestions on the related research work. Helpful discussions with Dr. Liu Likun at Telecommunication Satellite Branch of CAST are also acknowledged. This work was sponsored by the National Natural Science Foundation of China (No. 11272172).

Appendix A. The selected seven typical states are listed and illustrated in Table A1.

The inertia tensors of the typical states are (kg·m^2)

$$\boldsymbol{I}_{\mathrm{A}} = \begin{bmatrix} 15319 & -228 & -838 \\ -228 & 7012 & 53 \\ -838 & 53 & 16949 \end{bmatrix}$$

$$\boldsymbol{I}_{\mathrm{B}} = \begin{bmatrix} 16125 & -160 & -1722 \\ -160 & 8068 & 64 \\ -1722 & 64 & 17609 \end{bmatrix}$$

$$\boldsymbol{I}_{\mathrm{C}} = \begin{bmatrix} 18523 & -83 & -3081 \\ -83 & 10508 & 131 \\ -3081 & 131 & 18927 \end{bmatrix}$$

$$\boldsymbol{I}_{\mathrm{D}} = \begin{bmatrix} 22398 & 15 & -4933 \\ 15 & 14530 & 215 \\ -4933 & 215 & 21202 \end{bmatrix}$$

$$\boldsymbol{I}_{\mathrm{E}} = \begin{bmatrix} 17351 & -18 & -880 \\ -18 & 5713 & -275 \\ -880 & -275 & 13868 \end{bmatrix}$$

Table A1 The selected seven typical states.

Sequence	State	Description
1	E	Initial state
2	F	Big arm deployed
3	G	Big arm turned 90°
4	A	Small arm deployed/reflector in initial state
5	B	Reflector one third deployed (1/3)
6	C	Reflector two thirds deployed (2/3)
7	D	Reflector deployed and locked (final state)

$$\boldsymbol{I}_{\mathrm{F}} = \begin{bmatrix} 15333 & -346 & -877 \\ -346 & 4395 & 44 \\ -877 & 44 & 14444 \end{bmatrix}$$

$$\boldsymbol{I}_{\mathrm{G}} = \begin{bmatrix} 16485 & -131 & -795 \\ -131 & 4354 & -146 \\ -795 & -146 & 13240 \end{bmatrix}$$

where the subscript "A" denotes "State A", so as the other subscripts "B", "C", "D", "E", "F", and "G". The structural frequency matrices of the typical states are (rad/s)

$$\boldsymbol{\Omega}_{\mathrm{A}} = \mathrm{diag}(2.79, 2.95, 7.60, 10.98, 17.84, 24.55)$$

$$\boldsymbol{\Omega}_{\mathrm{B}} = \mathrm{diag}(0.79, 1.56, 2.38, 3.17, 4.50, 4.52)$$

$$\boldsymbol{\Omega}_{\mathrm{C}} = \mathrm{diag}(0.44, 0.70, 1.32, 2.03, 2.69, 3.38)$$

$$\boldsymbol{\Omega}_{\mathrm{D}} = \mathrm{diag}(0.79, 0.89, 2.07, 3.40, 5.56, 6.39)$$

$$\boldsymbol{\Omega}_{\mathrm{E}} = \mathrm{diag}(52.02, 59.81, 74.39, 81.51, 83.23, 92.62)$$

$$\boldsymbol{\Omega}_{\mathrm{F}} = \mathrm{diag}(4.18, 4.94, 6.37, 9.53, 10.38, 21.60)$$

$$\boldsymbol{\Omega}_{\mathrm{G}} = \mathrm{diag}(4.55, 4.92, 7.23, 9.49, 12.06, 25.45)$$

The rotational coupling coefficients of the typical deploying states are

$$\boldsymbol{F}_{\mathrm{A}} = \begin{bmatrix} -0.87 & 7.31 & 3.15 & 2.38 & -1.02 & 1.67 \\ -50.25 & -14.62 & -8.77 & 19.77 & 0.99 & 10.93 \\ 9.12 & 57.49 & -5.58 & 1.59 & -7.16 & 5.08 \end{bmatrix}$$

$$\boldsymbol{F}_{\mathrm{B}} = \begin{bmatrix} -20.43 & -3.63 & 2.55 & 13.53 & -0.49 & -2.90 \\ -2.36 & -62.78 & 22.38 & -3.18 & -17.31 & -28.10 \\ 49.72 & -4.99 & -0.17 & 51.81 & -10.41 & 4.06 \end{bmatrix}$$

$$\boldsymbol{F}_{\mathrm{C}} = \begin{bmatrix} -48.07 & -1.92 & 3.54 & 13.57 & 3.24 & -3.05 \\ -3.11 & -66.63 & 34.64 & -3.28 & 0.86 & -41.72 \\ 55.81 & -7.07 & 0.92 & 42.92 & -18.42 & -2.07 \end{bmatrix}$$

$$\boldsymbol{F}_{\mathrm{D}} = \begin{bmatrix} 4.36 & 8.37 & -59.04 & -3.15 & -23.33 & -1.57 \\ 103.49 & 6.49 & 2.67 & -55.28 & 0.99 & -6.70 \\ 7.23 & -108.56 & -40.97 & 1.34 & -16.36 & -1.17 \end{bmatrix}$$

$$\boldsymbol{F}_{\mathrm{E}} = \begin{bmatrix} -2.11 & 13.17 & 0.16 & 0.11 & 0.51 & 0.10 \\ 14.19 & 1.89 & 1.87 & -0.40 & -4.65 & -3.45 \\ -0.74 & -5.73 & 2.25 & -4.15 & -1.60 & 0.41 \end{bmatrix}$$

$$\boldsymbol{F}_{\mathrm{F}} = \begin{bmatrix} 7.86 & 3.87 & 4.84 & -0.23 & -2.27 & -0.12 \\ -4.92 & -31.70 & -3.36 & 9.85 & -10.14 & -4.97 \\ 22.75 & 0.73 & 28.30 & -3.45 & 2.61 & 0.26 \end{bmatrix}$$

$$\boldsymbol{F}_{\mathrm{G}} = \begin{bmatrix} -2.99 & -16.28 & -1.585 & -1.26 & 3.89 & 0.92 \\ -17.36 & 5.07 & -32.69 & -6.63 & -1.07 & 2.67 \\ 0.08 & -34.74 & 4.45 & 11.31 & 4.83 & 3.68 \end{bmatrix}$$

References

1. Angeletti P, Lisi M, Lucchi G. Satellite antennas for broadband mobile communications missions; 2003. Report No.: AIAA-2003-2222.
2. Soykasap O, Pellegrino S, Howard P, Notter M. Folding large antenna tape spring. *J Spacecraft Rockets* 2008;**45**(3):560–7.
3. Koduru C, Tomei B, Sichi S, Suh K, Ha T. Advanced space based network using ground based beam former; 2011. Report No.: AIAA-2011-8077.
4. Datashvili L, Baier H, Wehrle E, Kuhn T, Hoffmann J. Large shell-membrane space reflectors; 2010. Report No.: AIAA-2010-2504.
5. Montgomery VI E E, Johnson L. The development of solar sail propulsion for NASA science missions to the inner solar system; 2004. Report No.: AIAA-2004-1506.
6. Macdonald M, McInnes C, Hughes G. Technology requirements of exploration beyond neptune by solar sail propulsion. *J Spacecraft Rockets* 2010;**47**(3):472–83.
7. Thomas S, Paluszek M, Wie B, Murphy D. AOCS performance and stability validation for large flexible solar sail spacecraft; 2005. Report No.: AIAA-2005-3926.
8. Lane SA, Murphey TW, Zatman M. Overview of the innovative space-based radar antenna technology program. *J Spacecraft Rockets* 2011;**48**(1):135–45.
9. Ruqqiero EJ, Inman DJ. Gossamer spacecraft: recent trends in design, analysis, experimentation, and control. *J Spacecraft Rockets* 2006;**43**(1):10–24.
10. Meguro A, Ishikawa H, Tsujihata A. Study on ground verification for large deployable modular structures. *J Spacecraft Rockets* 2006;**43**(4):780–7.
11. Likins PW. Dynamics and control of flexible space vehicles; 1970. Report No.: JPL Technical Report 32-1329.
12. Nagashio T, Kida T, Ohtani T, Hamada Y. Design and implementation of robust symmetric attitude controller for ETS-VIII spacecraft. *Control Eng Pract* 2010;**18**(12):1440–51.
13. Yonezawa K, Homma M. Attitude control on ETS-VIII mobile communication satellite with large deployable antenna; 2003. Report No.: AIAA-2003-2216.
14. Kida T, Yamaguchi I, Chida Y, Sekiguchi T. On-orbit robust control experiment of flexible spacecraft ETS-VI. *J Guid Control Dyn* 1997;**20**(5):865–72.
15. Wie B, Liu Q, Bauer F. Classical and robust H_∞ control redesign for the Hubble Space Telescope. *J Guid Control Dyn* 1993;**16**(6):1069–77.
16. Liu JY, Bender DJ, Chiang RY, Chen S, Wang W. Innovative SBR antenna technology (ISAT) ACS design; 2008. Report No.: AIAA-2008-7231.
17. Craig Jr RR, Bampton MCC. Coupling of substructures for dynamic analyses. *AIAA J* 1968;**6**(7):1313–9.
18. Craig Jr RR, Hale AL. Block-Krylov component synthesis method for structural model reduction. *J Guid Control Dyn* 1988;**11**(6):562–70.
19. Young KD. Distributed finite-element modeling and control approach for large flexible structures. *J Guid Control Dyn* 1990;**13**(4):703–13.
20. Ghosh T. Improved method of modal synthesis in the analysis of International Space-Station structures; 1997. Report No.: AIAA-1997-1038.
21. Ghosh T. Improved method of generating control system model using modal synthesis; 1997. Report No.: AIAA-1997-3673.
22. Newsom JR, Anderson WW. The NASA-LaRC Controls-Structures Interaction (CSI) technology program. *Control Eng Pract* 1994;**2**(3):479–90.
23. Byun KW, Wie B, Sunkel J. Robust non-minimum-phase compensation for a class of uncertain dynamical systems. *J Guid Control Dyn* 1991;**14**(6):1191–9.
24. Wie B, Gonzalez M. Control synthesis for flexible space structures excited by persistent disturbances. *J Guid Control Dyn* 1992;**15**(5):73–80.
25. Zhou FQ, Zhao C, Zhou J. Robust H_∞ design of the attitude control / momentum management system for a space station. *Chinese J Aeronaut* 1999;**12**(4):227–30.
26. Wu YWA, Chiang RY, Li RK. Precision beacon-assisted attitude control for spaceway; 2003. Report No.: AIAA-2003-5829.
27. Fowell RA, Wang HG. Precision pointing of the Thuraya satellite. In: *Proceedings of the 26th annual AAS rocky mountain guidance and control conference*; 2003. p. 455–69.
28. Charbonnel C. H_∞ controller design and μ analysis: powerful tools for flexible satellite attitude control; 2010. Report No.: AIAA-2010-7907.
29. Yu L. *Robust control – LMI approach*. Tsinghua University Press; 2002: 31–32 [Chinese].

Xing Zhigang is a Ph.D. student in the School of Aerospace at Tsinghua University. He received his B.S. degree from Harbin Institute of Technology in 2008. His area of research includes dynamics and control.

Zheng Gangtie received his Ph.D. degree in mechanics from Harbin Institute of Technology in 1988. Now he is a professor in the School of Aerospace at Tsinghua University. His main research interests are structural design, dynamics, and control.